Comparative CFD Analysis of Conventional and Blended Winglets for a Subsonic Electric Regional Aircraft Wing

a project presented to
The Faculty of the Department of Aerospace Engineering
San José State University

in partial fulfillment of the requirements for the degree of

Master of Science in Aerospace Engineering

by

Matteen Tabrizi

May 2026

approved by

Dr. Periklis Papadopoulos
Faculty Advisor



© 2026

Matteen Tabrizi

ALL RIGHTS RESERVED

ABSTRACT

Battery-electric aircraft are range-limited by the energy density of current battery technologies. Reducing induced drag through wingtip devices, such as winglets, split tips, and sharklets, can improve the lift-to-drag ratio at subsonic speeds. This study uses computational fluid dynamics at Mach 0.4 and an altitude of approximately 5 km to compare the aerodynamic performance of a baseline wing, a conventional winglet, and a blended-winglet configurations having 45° sweep angle and 45° cant angle, at angles of attack of 0°, 6°, and 10°. Changes in C_L, C_D, and L/D, along with the surface-pressure, wall-shear-stress, and near-tip wake distributions, are evaluated for each configuration. The conventional winglet produced the highest lift-to-drag ratio at each angle of attack, with the greatest aerodynamic efficiency occurring at 6°.

ACKNOWLEDGEMENTS

I would like to express sincere gratitude to Dr. Papadopoulos for his invaluable guidance and expertise throughout the course of this project. In addition, I would like to extend my appreciation to the San José State University Aerospace Engineering Department for providing the resources and support that made this work possible. I also want to thank my mother and father for their unconditional support throughout my academic journey.

Contents

Abstract iii

Acknowledgements iv

List of Figures ix

List of Tables x

Symbols xi

1 Introduction 1
- 1.1 Motivation . . . 1
- 1.2 Literature Review . . . 1
- 1.3 Project Proposal . . . 5

2 Methodology 7

3 Governing Equations 8
- 3.1 Drag Coefficients and Induced Drag . . . 8
- 3.2 Continuity Equation . . . 8
- 3.3 Navier-Stokes Equations . . . 9

4 Wing Geometry 10
- 4.1 NACA 63-418 Airfoil . . . 11
- 4.2 Geometry of 45-45 Conventional Winglet . . . 12
- 4.3 Geometry of 45-45 Blended Winglet . . . 14

5 Computational Domain and Boundary Conditions 16

6 Mesh 17

7 Results 20
- 7.1 Baseline Configuration at 0° Angle of Attack . . . 20
- 7.2 Baseline Configuration at 6° Angle of Attack . . . 23
- 7.3 Baseline Configuration at 10° Angle of Attack . . . 26
- 7.4 45-45 Winglet Configuration at 0° Angle of Attack . . . 29
- 7.5 45-45 Winglet Configuration at 6° Angle of Attack . . . 33
- 7.6 45-45 Winglet Configuration at 10° Angle of Attack . . . 35
- 7.7 45-45 Blended-Winglet Configuration at 0° Angle of Attack . . . 38
- 7.8 45-45 Blended-Winglet Configuration at 6° Angle of Attack . . . 41
- 7.9 45-45 Blended-Winglet Configuration at 10° Angle of Attack . . . 44
- 7.10 Overview of Results . . . 47

8 Verification and Validation 49

9 Conclusion 52

References 53

List of Figures

1.1 Domain of the rectangular channel showing the inlet, outlet, symmetry plane, and extension regions with the vortex generator mounted on the bottom [2]. 2
1.2 Wing modifications and test cases: VG - vortex generator; TVG - triangle vortex generator; RVG - rectangle vortex generator [3]. 3
1.3 Winglet geometry showing key parameters: tip chord, root chord, sweep, span, radius, and angle of attack (AoA) [4]. 3
1.4 Example of winglet cant-angle variation, showing cant measured from a horizontal reference line [6]. 4
1.5 Surface and volume mesh of the wing-winglet configuration, showing refinement near the leading edge and tip region [11]. 5
1.6 Effect of winglet dihedral angle on induced drag [12]. 6
1.7 Effect of winglet toe-out angle on induced drag [12]. 6
4.1 Wing geometry used in the simulations, showing the tapered, low-sweep planform and key dimensions (span, root chord, and tip chord). 11
4.2 Geometry of the NACA 63-418 airfoil used for the wing, based on coordinates from AirfoilTools [18]. 12
4.3 Isometric view of the conventional winglet configuration. 12
4.4 Top view of the conventional winglet configuration. 13
4.5 Side view of the conventional winglet configuration. 13
4.6 Head-on view showing the geometric dimensions of the conventional winglet. . . . 13
4.7 Top view showing the geometric dimensions of the conventional winglet. 14
4.8 Top view of the 45-45 blended-winglet configuration. 15
4.9 Side view of the 45-45 blended-winglet configuration. 15
4.10 Isometric view of the 45-45 blended-winglet configuration. 15
5.1 Sectional view of the computational domain showing the airfoil position relative to the global coordinate axes. 16
6.1 Finite element mesh generated in Ansys 2025 R2. 17
6.2 Computational mesh around the wing section. 18
6.3 Refined computational mesh near the wing surface. 18
6.4 Inflation layers near the wing surface. 19
6.5 Close-up view of the inflation layers near the wing trailing edge. 19
7.1 Coefficient of drag convergence plot at 0° angle of attack for the baseline configuration. 20
7.2 Coefficient of lift convergence plot at 0° angle of attack for the baseline configuration. 21
7.3 Wall shear contour at 0° angle of attack for the baseline configuration. 21
7.4 Pressure contour at 0° angle of attack for the baseline configuration. 22
7.5 Swirling-strength contour of the near-tip wake for the baseline-wing configuration at 0° angle of attack. 23
7.6 Coefficient of drag convergence plot at 6° angle of attack for the baseline configuration. 24
7.7 Coefficient of lift convergence plot at 6° angle of attack for the baseline configuration with the new reference area. 24
7.8 Pressure contour at 6° angle of attack for the baseline configuration. 25
7.9 Swirling-strength contour of the near-tip wake for the baseline-wing configuration at 6° angle of attack. 25

7.10 Wall shear contour at 6° angle of attack for the baseline configuration with the new reference area. 26
7.11 Drag-coefficient convergence history for the baseline wing configuration at 10° angle of attack. 27
7.12 Lift-coefficient convergence history for the baseline wing configuration at 10° angle of attack. 27
7.13 Pressure distribution over the baseline wing configuration at 10° angle of attack. . . 28
7.14 Wall-shear-stress distribution over the baseline wing configuration at 10° angle of attack. 28
7.15 Swirling-strength contour of the near-tip wake for the baseline-wing configuration at 10° angle of attack. 29
7.16 Lift-coefficient convergence history for the 45-45 winglet configuration at 0° angle of attack. 30
7.17 Drag-coefficient convergence history for the 45-45 winglet configuration at 0° angle of attack. 30
7.18 Wall shear stress distribution for the conventional winglet configuration at 0° angle of attack. 31
7.19 Pressure contour at 0° angle of attack for the 45-45 winglet configuration. 32
7.20 Swirling-strength contour of the near-tip wake for the conventional-winglet configuration at 0° angle of attack. 32
7.21 Wall shear stress contour at 6° angle of attack for the 45-45 winglet configuration. . 33
7.22 Swirling-strength contour of the near-tip wake for the conventional-winglet configuration at 6° angle of attack. 34
7.23 Pressure contour at 6° angle of attack for the 45-45 winglet configuration. 34
7.24 Lift-coefficient iteration history for the 45-45 winglet configuration at 10° angle of attack. 35
7.25 Drag-coefficient iteration history for the 45-45 winglet configuration at 10° angle of attack. 36
7.26 Pressure distribution over the 45-45 winglet configuration at 10° angle of attack. . . 36
7.27 Wall-shear-stress distribution over the 45-45 winglet configuration at 10° angle of attack. 37
7.28 Swirling-strength contour of the near-tip wake for the conventional-winglet configuration at 10° angle of attack. 37
7.29 Drag-coefficient convergence history for the 45-45 blended-winglet configuration at 0° angle of attack. 38
7.30 Lift-coefficient convergence history for the 45-45 blended-winglet configuration at 0° angle of attack. 39
7.31 Pressure contour for the 45-45 blended-winglet configuration at 0° angle of attack. . 40
7.32 Swirling-strength contour of the near-tip wake for the blended-winglet configuration at 0° angle of attack. 40
7.33 Wall shear stress contour for the 45-45 blended-winglet configuration at 0° angle of attack. 41
7.34 Drag-coefficient convergence history for the 45-45 blended-winglet configuration at 6° angle of attack. 42

7.35 Lift-coefficient convergence history for the 45-45 blended-winglet configuration at 6° angle of attack. 42
7.36 Swirling-strength contour of the near-tip wake for the blended-winglet configuration at 6° angle of attack. 43
7.37 Pressure distribution over the 45-45 blended-winglet configuration at 6° angle of attack. 43
7.38 Wall-shear-stress distribution over the 45-45 blended-winglet configuration at 6° angle of attack. 44
7.39 Lift-coefficient iteration history for the 45-45 blended-winglet configuration at 10° angle of attack. 45
7.40 Drag-coefficient iteration history for the 45-45 blended-winglet configuration at 10° angle of attack. 45
7.41 Pressure distribution over the 45-45 blended-winglet configuration at 10° angle of attack after 1000 iterations. 46
7.42 Wall-shear-stress distribution over the 45-45 blended-winglet configuration at 10° angle of attack after 1000 iterations. 46
7.43 Swirling-strength contour of the near-tip wake for the blended-winglet configuration at 10° angle of attack. 47
8.1 Comparison of lift coefficient as a function of angle of attack for the baseline wing, 45-45 winglet, and 45-45 blended-winglet configurations. Published clean NACA 63_3-418 airfoil wind-tunnel data at $Re = 5 \times 10^6$ were included as a qualitative reference. The published data represented a two-dimensional airfoil, whereas the CFD results represented three-dimensional finite-wing configurations. 49
8.2 Drag coefficient convergence history for the baseline wing at 6° angle of attack. . . 50
8.3 Lift coefficient convergence history for the baseline wing at 6° angle of attack. . . . 50

List of Tables

7.1 Aerodynamic coefficients for the baseline configuration at 0° angle of attack. 20
7.2 Aerodynamic coefficients for the baseline configuration at 6° angle of attack. 23
7.3 Aerodynamic coefficients for the baseline configuration at 10° angle of attack. . . . 27
7.4 Aerodynamic coefficients for the conventional non-blended winglet configuration with a 45° cant angle and 45° sweep angle at 0° angle of attack. 29
7.5 Aerodynamic coefficients for the 45-45 winglet configuration at 6° angle of attack. . 33
7.6 Aerodynamic coefficients for the 45-45 winglet configuration at 10° angle of attack. 35
7.7 Aerodynamic coefficients for the 45-45 blended-winglet configuration at 0° angle of attack. 38
7.8 Aerodynamic coefficients for the 45-45 blended-winglet configuration at 0° angle of attack. 39
7.9 Aerodynamic coefficients for the 45-45 blended-winglet configuration at 6° angle of attack. 41
7.10 Iteration-averaged aerodynamic coefficients for the 45-45 blended-winglet configuration at 10° angle of attack. 45
7.11 Comparison of aerodynamic coefficients for the baseline, 45-45 winglet, and 45-45 blended-winglet configurations at 0° angle of attack. 47
7.12 Comparison of aerodynamic coefficients for the baseline, 45-45 winglet, and 45-45 blended-winglet configurations at 6° angle of attack. 48
7.13 Comparison of aerodynamic coefficients for the baseline, 45-45 winglet, and 45-45 blended-winglet configurations at 10° angle of attack. 48

Symbols

Symbol	Definition	Units (SI)
C_D	Drag coefficient	-
C_L	Lift coefficient	-
C_{D_i}	Induced drag coefficient	-
D	Drag force	N
L	Lift force	N
L/D	Lift-to-drag ratio	-
S	Wing reference area	m^2
V	Freestream velocity	m/s
W	Weight	N
AR	Aspect ratio (b^2/S)	-
e	Oswald efficiency factor	-

Greek Symbols

α	Angle of attack	deg or rad
ρ	Air density	kg/m^3

Subscripts

$(\cdot)_D$	Drag	-
$(\cdot)_L$	Lift	-

Acronyms

CFD	Computational Fluid Dynamics	-

1. Introduction

Electric aircraft are emerging as a solution for sustainable regional and commuter aviation. However, compared to conventional jets, batteries are far less powerful than the fuel used in gas-fueled aircraft, which severely limits range. Therefore, improving aerodynamic efficiency becomes critical. One promising approach is the use of winglets.

This study uses Computational Fluid Dynamics (CFD) to evaluate how winglets designs influence drag for electric aircraft. The goal is to redistribute lift and weaken wingtip vortices, lowering induced drag.

1.1 Motivation

Battery electric aircraft promise quieter and lower-emission flying, but they are constrained by today's battery technology. Aviation is a challenging sector for decarbonization, which relies on aerodynamic efficiency that allows for extended range. Challenges facing subsonic aircraft such as electric aircraft include induced drag. As a solution, wingtip devices help weaken tip vortices and improve lift-to-drag ratio. This project uses computational fluid dynamics to quantify how winglets redistribute lift and cut induced drag.

1.2 Literature Review

Electric aircraft are emerging as sustainable solutions for regional and commuter aviation, but their operational range is limited by the relatively low energy density of current battery technologies. Since electric aircraft cannot provide the same endurance and speed as conventional gas-fueled aircraft, optimizing aerodynamic efficiency becomes essential to extend range and reduce power consumption. This includes reducing induced drag through non-planar wing configurations such as winglets, toe-out and cant angles, dihedral angles, and sweep geometries. Computational fluid dynamics (CFD) has become a powerful tool to analyze the effects of geometry on wings. Induced drag is important to consider because it accounts for a large portion of total drag in subsonic flight. Wingtip vortices are a primary source of induced drag in aircraft.

A recent review by Sundaram et al. [1] analyzes several winglet design configurations and how they can reduce induced drag in electric aircraft. The review highlights that induced drag constitutes a major portion of total drag at subsonic speeds. Optimized wingtip devices can improve range and endurance. The most effective configurations in reducing induced drag are blended winglets, sharklets, and split-tip winglets. Blended winglets offer a smooth transition between the wing and tip device, which reduces interference drag and improves the lift-to-drag ratio. Sharklets provide efficient vortex control, whereas split-tip winglets improve aerodynamic efficiency by combining upward and downward strakes to manage upper and lower vortices. The study also evaluates cant, toe, and sweep angles, determining that cant angle has the strongest effect on performance. In particular, moderate cant angles (0–45°) provide the best trade-off between drag reduction and structural loading. According to Sundaram et al. [1], these configurations achieve a 3-6% reduction in total drag, with even greater relative reductions predicted for electric aircraft operating at lower speeds. The review concludes that upward-canted sharklet designs are the most suitable for smaller electric aircraft.

Geometric shaping plays a similarly important role. Lu and Zhou [2] conduct numerical simulations comparing curved and planar winglet designs. Their study demonstrates that geometry and angle selection are critical in controlling vortex strength and overall aerodynamic behavior. In their setup, a pair of winglets are installed at an attack angle of $\beta = 45°$ and positioned $P = 170\,\text{mm}$ downstream of the inlet, a placement chosen specifically to allow the inlet flow to become fully developed and stable before interacting with the winglets Using the Field Synergy Principle to examine flow– pressure gradient alignment, they conclude that curved trapezoidal winglets provide the best balance of drag reduction and flow efficiency when paired with a 45° angle of attack and a 20° inclination angle. This configuration reduces pressure gradients in the junction region, thereby reducing vortex strength and improving aerodynamic performance

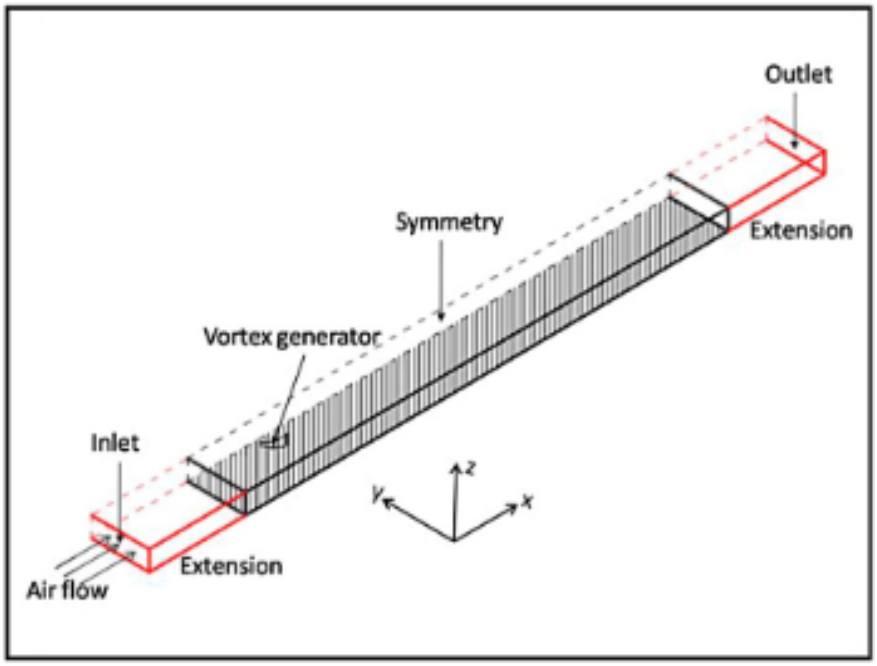


Figure 1.1: Domain of the rectangular channel showing the inlet, outlet, symmetry plane, and extension regions with the vortex generator mounted on the bottom [2].

Orientation-based modifications have also shown strong aerodynamic influence. Hasan et al. [3] study different wing configurations with 45° and 90° winglets using CFD software at a Reynolds number of approximately 360,000. Their results show that 45° winglets are more aerodynamically efficient than 90° winglets, particularly at higher angles of attack. The presence of vortex generators improves lift by up to 20%. This work demonstrates the significance of winglet orientation in improving aerodynamic efficiency.

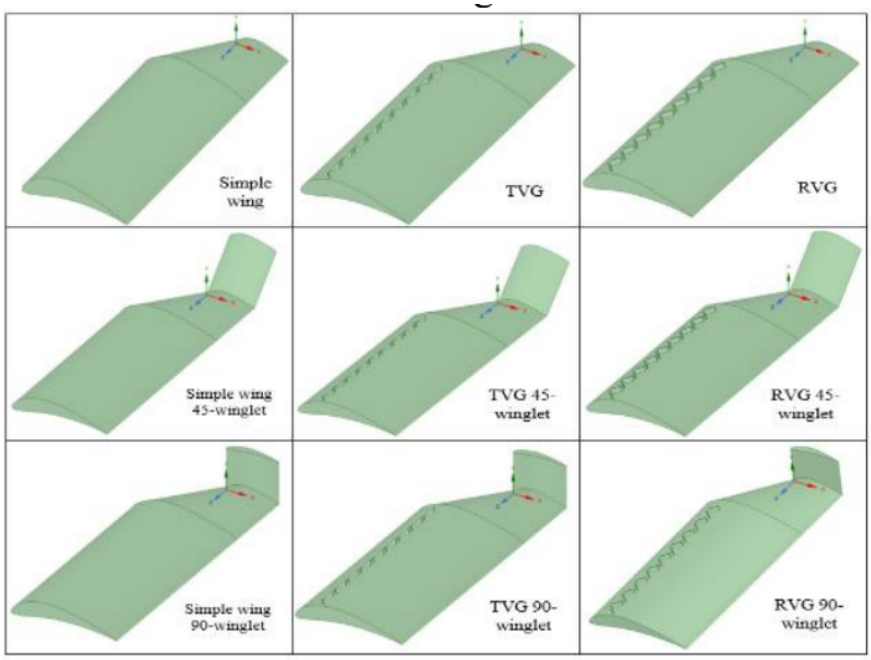


Figure 1.2: Wing modifications and test cases: VG - vortex generator; TVG - triangle vortex generator; RVG - rectangle vortex generator [3].

Additional geometric alterations, such as introducing a mid-height slot within a winglet, have also proven effective. Babu et al. [4] perform a CFD study comparing a plain wing, a wing with a traditional winglet, and a wing with a slotted winglet. The study uses a validated RANS setup in Ansys Fluent with the Spalart-Allmaras turbulence model, simulating angles of attack from $-4°$ to $12°$ at 20 m/s and 270 m/s. The slotted winglet design allows a small amount of air to pass through the mid-height slot, weakening the tip vortex and reducing drag. The authors report approximately a 4% increase in lift-to-drag ratio for traditional winglets and roughly 3.16% for slotted winglets, indicating improved aerodynamic efficiency and reduced energy consumption.

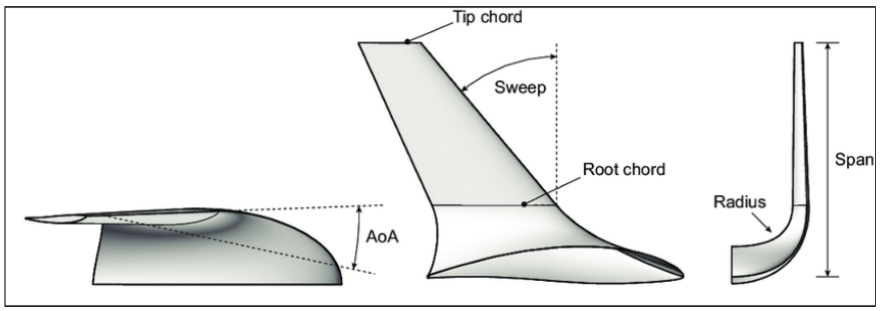


Figure 1.3: Winglet geometry showing key parameters: tip chord, root chord, sweep, span, radius, and angle of attack (AoA) [4].

Madani et al. [5] conducted a CFD investigation of blended winglets to determine how cant angle influences aerodynamic performance. Cant angles ranged from $-90°$ to $90°$, and their results demonstrated that cant angles significantly affects the wingtip vortex by altering its strength and

position. The 90° cant-angle winglet produced the highest lift-to-drag ratio; however, aerodynamic benefits were present at moderate angles of attack as well. Beyond orientation alone, surface shaping contributes meaningfully to winglet performance. Farook and Chitharanjan [6] compare raked winglets with and without corrugation added to the tip. Their model uses a NACA 2412 tapered wing with a winglet span of 10% of the total wingspan, a raked sweep of 26°, and a blended cant of 30°. Corrugation reduces drag and increases lift at moderate to high angles of attack, providing approximately 7% more lift than a conventional wing and 2% more than a raked winglet without corrugation.

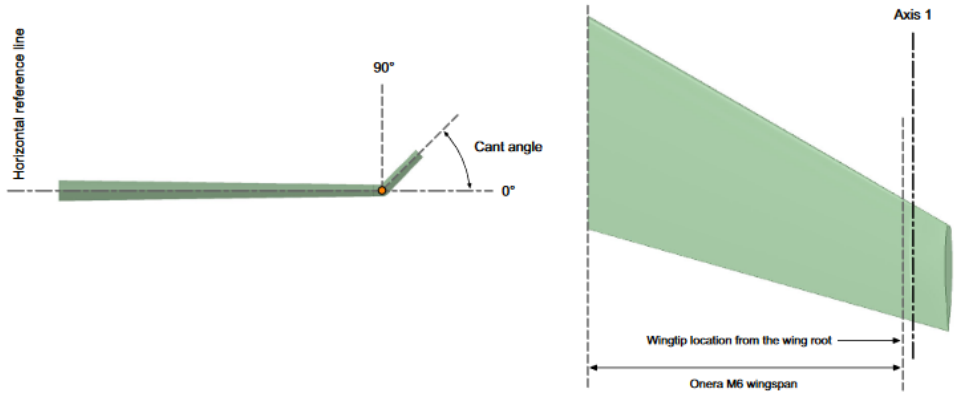


Figure 1.4: Example of winglet cant-angle variation, showing cant measured from a horizontal reference line [6].

A systematic evaluation of cant and sweep further highlights the aerodynamic richness of winglet design. Guerrero et al. [7] study variable-cant winglets on the ONERA-M6 wing using RANS turbulence modeling. Cant angles of 0°, 15°, 45°, and 80° are evaluated at multiple Mach numbers. Their results show that moderate cant angles improve aerodynamic efficiency at both low and high subsonic speeds, while extreme cant angles (≈80°) increase parasite drag and reduce maximum lift. Increasing sweep to 60° also reduces drag at high subsonic Mach numbers.

Research focused specifically on electric aircraft reveals geometry-dependent behavior not always observed on conventional transport wings. Malathi [8] demonstrates that winglets significantly improve the performance of an electric trainer wing at low subsonic speeds. Simulations at 55 m/s and a 5° angle of attack demonstrate that downward-facing sharklets increase lift by 12% and reduce drag by 46.6%. Upward sharklets also improve performance, while split-tip winglets are less effective.

While aerodynamic benefits dominate most discussions, structural and aeroelastic considerations cannot be overlooked. Pecora et al. [9] analyze morphing camber winglets using aeroelastic modeling. Their design uses actuated flap tabs, a doublet-lattice aerodynamic model, and vibration-mode-based flutter analysis. The results show that appropriate mass balancing prevents flutter up to 1.25 V_D, while excessive winglet mass shifts the flutter boundary downward, restricting flight speed.

Moreover, Sheneshen and Kamal [10] study blended wing-body transport configurations using XFLR5 to evaluate winglet design influences on aerodynamic efficiency and static stability. They vary span, taper, cant, sweep, and toe angles, and find that reduced cant angles generally improve lift-curve slope, L/D ratio, and minimize $C_{D,\min}$. Notably, the lowest $C_{D,\min}$ occurs for a wing without

winglets, demonstrating that winglets add profile drag even when improving overall performance.

Optimization-driven studies provide deeper insight into the multidimensional nature of winglet design. Heidari Soreshjani and Jahangirian [11] conduct a high-fidelity CFD optimization study on the DLR-F6 wing at Mach 0.4 and 5 km altitude. They vary winglet length, twist, cant, sweep, taper, and blend radius, identifying optimized designs that reduce drag by approximately 9% and increase lift-to-drag ratio by about 10%. The optimized winglet decreases vortex size and generates a small forward component of lift near the tip.

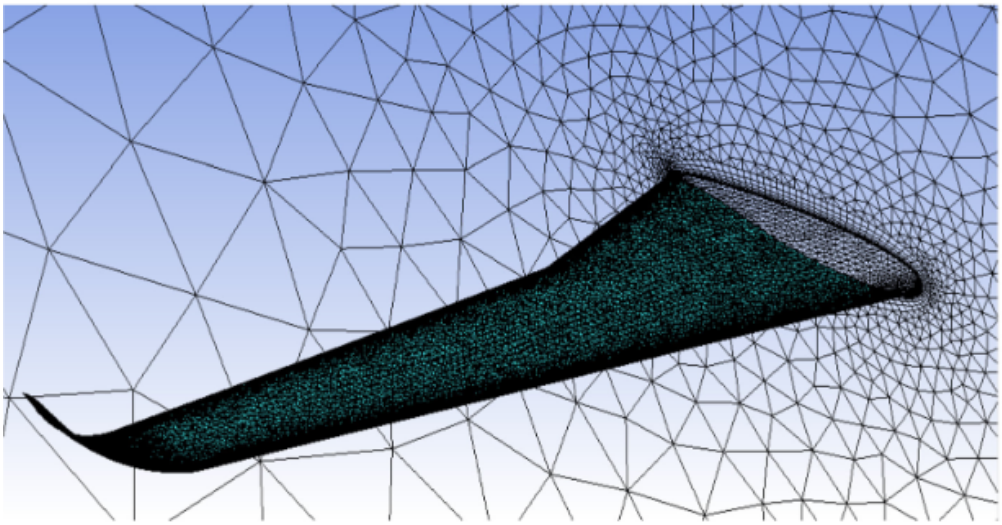


Figure 1.5: Surface and volume mesh of the wing-winglet configuration, showing refinement near the leading edge and tip region [11].

Further insight into the sensitivity of induced drag to winglet geometry comes from studies that investigate large parametric design spaces, rather than isolated geometric variations. Kim [12] conducts a parametric optimization study of wing-tip designs for the Boeing 747-100, testing 108 configurations across multiple dihedral and toe-out angles. All configurations achieve at least an 8% reduction in induced drag, with the Whitcomb winglet providing the largest reduction at approximately 11%.

Beyond transport aircraft, similar optimization principles have been applied to high-efficiency platforms such as sailplanes, where even small improvements in aerodynamic performance are meaningful. Krebs and Bramesfeld [13] demonstrate that a multi-objective optimization strategy produces more effective winglet designs for sailplanes than traditional experience-based methods. Their final design improves average speed by up to 1.5% and increases bending moment by only 0.5%.

1.3 Project Proposal

The objective of this study is to evaluate and compare the aerodynamic performance of three wing configurations representative of a subsonic electric regional aircraft. The configurations to be investigated are a baseline wing without a wingtip device, a conventional 45-45 winglet configuration, and a 45-45 blended-winglet configuration.

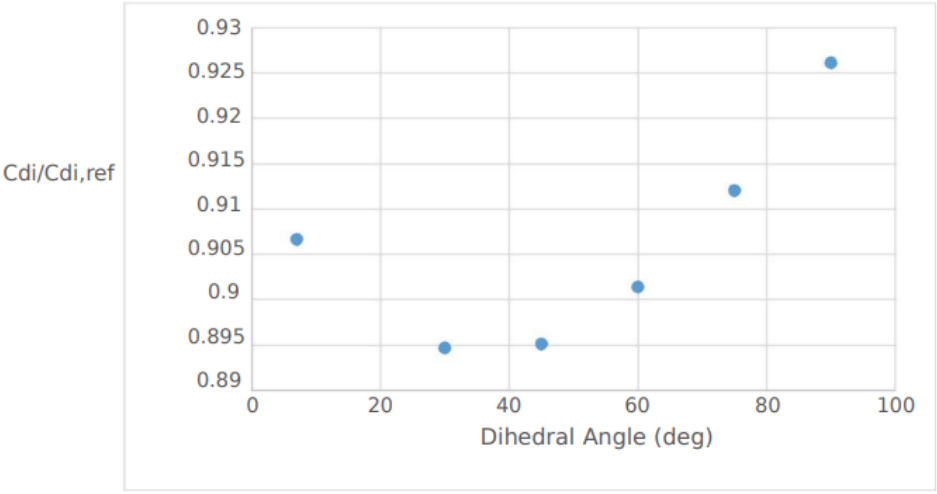


Figure 1.6: Effect of winglet dihedral angle on induced drag [12].

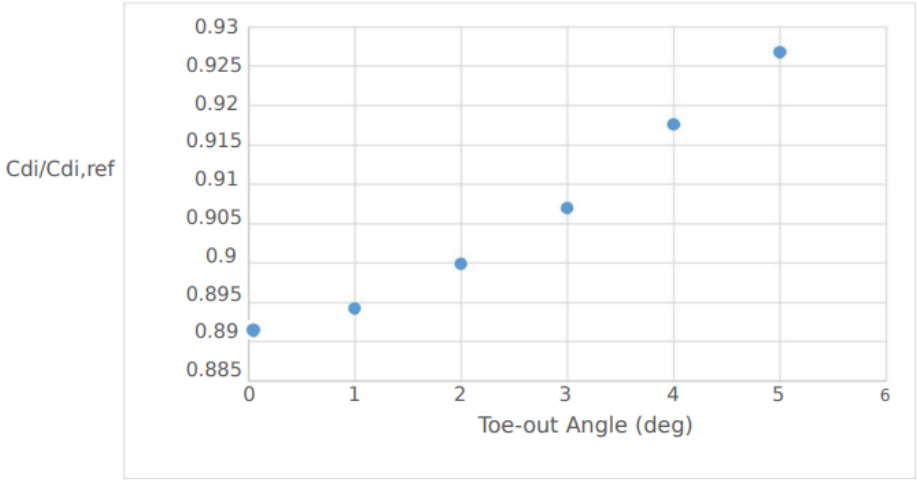


Figure 1.7: Effect of winglet toe-out angle on induced drag [12].

Each configuration is evaluated at angles of attack of 0°, 6°, and 10°. The freestream conditions are maintained at a Mach number of $M = 0.4$ and an altitude of approximately 5,000 m. A reference area of 15.525 m^2 is used consistently for all configurations when running the simulations and calculating the aerodynamic coefficients.

The primary purpose of the investigation is to determine how the addition and geometric blending of a winglet influence the aerodynamic performance of the baseline wing. From each CFD solution, the lift coefficient (C_L), total drag coefficient (C_D), and lift-to-drag ratio (L/D) are obtained.

In addition, the surface-pressure distribution, wall-shear-stress distribution, and vortex in near-tip wake are examined. These flow-field results are used to assess how the conventional and blended winglets affect aerodynamic loading and wingtip-vortex development relative to the baseline wing.

2. Methodology

Simulations are run in Ansys Fluent. The SST k-ω turbulence model is used to model the flow around the wing and winglet surfaces. Three configurations are investigated: the baseline wing without a wingtip device, a conventional 45-45 winglet configuration, and a 45-45 blended-winglet configuration.

Each configuration is simulated at angles of attack of 0°, 6°, and 10°. The freestream conditions are maintained at a Mach number of 0.4 and an altitude of approximately 5 km. The angle of attack is imposed by adjusting the freestream velocity components while maintaining a constant velocity magnitude for all cases. A reference area of 15.525 m^2 is used consistently when calculating the aerodynamic coefficients.

The computational domain consists of a pressure-far-field-inlet boundary, a pressure-outlet boundary, and outer boundaries designated as far-field walls to reduce their influence on the near-field flow. The wing and winglet surfaces are defined as no-slip walls.

A quad-dominant unstructured mesh is created, with triangular elements used around curved regions. Local refinement is applied near the leading edge, trailing edge, wingtip, and winglet surfaces. Fifteen inflation layers are placed along the aerodynamic surfaces, with a first-layer height of 1.0×10^{-3} m and a growth rate of 1.18, to improve the resolution of the near-wall velocity gradients.

The lift-to-drag ratio is subsequently calculated as

$$\frac{L}{D} = \frac{C_L}{C_D}. \tag{2.1}$$

Solution convergence is evaluated using the residual histories and the stabilization of the monitored lift and drag coefficients. In addition to the aerodynamic coefficients, surface-pressure distributions, wall-shear-stress, and swirling strength of vortex structures are examined to compare the aerodynamic behavior of the three configurations.

3. Governing Equations

The governing equations for this study are based on the principles of fluid mechanics, namely the continuity and Navier-Stokes equations. These equations describe the conservation of mass and momentum for a viscous, compressible fluid such as air at subsonic speeds.

3.1 Drag Coefficients and Induced Drag

The drag force on an aircraft body may be expressed by the well-known drag equation:

$$D = \frac{1}{2}\rho V^2 A C_D, \tag{3.1}$$

where D is the drag force, ρ is the air density, V is freestream velocity, A is the reference area, and C_D is the drag coefficient. The drag coefficient, therefore, takes into account the complex dependencies of drag on shape, inclination, viscous and compressibility effects [14].

For lifting wings, the total drag coefficient may be split into a zero-lift term C_{D0} and the induced-drag component C_{D_i}:

$$C_D = C_{D0} + C_{D_i}. \tag{3.2}$$

Based on lifting-line theory, the induced drag coefficient is given by:

$$C_{D_i} = \frac{C_L^2}{\pi A R e}, \tag{3.3}$$

where C_L is the lift coefficient, AR is the wing's aspect ratio (span^2/area), and e is the Oswald efficiency factor (typically $e \leq 1.0$).

Alternatively, the general parabolic drag polar may be written:

$$C_D = C_{D0} + K C_L^2, \tag{3.4}$$

where $K = 1/(\pi A R e)$.

By substituting into the drag equation, the induced drag force may be expressed as:

$$D_i = \frac{1}{2}\rho V^2 A \frac{C_L^2}{\pi A R e}, \tag{3.5}$$

which clearly shows that induced drag grows with the square of the lift coefficient and declines with increasing aspect ratio and efficiency.

Note: $AR = b^2/S$ where b is span and S is wing planform area.

3.2 Continuity Equation

The continuity equation focuses on mass conservation, stating that the rate of change of mass within a control volume is equal to the net mass flux through its surface. In other words, mass can only

change inside a control volume if mass flows in or out:

$$\frac{\partial \rho}{\partial t} + \nabla \cdot (\rho \mathbf{u}) = 0. \tag{3.6}$$

Expanding this in Cartesian coordinates gives:

$$\frac{\partial \rho}{\partial t} + \frac{\partial (\rho u)}{\partial x} + \frac{\partial (\rho v)}{\partial y} + \frac{\partial (\rho w)}{\partial z} = 0. \tag{3.7}$$

3.3 Navier-Stokes Equations

The flow is modeled using the compressible Navier-Stokes equations, which express the conservation of momentum for a viscous fluid. These equations account for convective transport, pressure gradients, and viscous stresses in the fluid domain.

X-Momentum:

$$\frac{\partial (\rho u)}{\partial t} + \frac{\partial (\rho u^2)}{\partial x} + \frac{\partial (\rho uv)}{\partial y} + \frac{\partial (\rho uw)}{\partial z} = -\frac{\partial p}{\partial x} + \frac{1}{Re}\left(\frac{\partial \tau_{xx}}{\partial x} + \frac{\partial \tau_{xy}}{\partial y} + \frac{\partial \tau_{xz}}{\partial z}\right). \tag{3.8}$$

Y-Momentum:

$$\frac{\partial (\rho v)}{\partial t} + \frac{\partial (\rho uv)}{\partial x} + \frac{\partial (\rho v^2)}{\partial y} + \frac{\partial (\rho vw)}{\partial z} = -\frac{\partial p}{\partial y} + \frac{1}{Re}\left(\frac{\partial \tau_{xy}}{\partial x} + \frac{\partial \tau_{yy}}{\partial y} + \frac{\partial \tau_{yz}}{\partial z}\right). \tag{3.9}$$

Z-Momentum:

$$\frac{\partial (\rho w)}{\partial t} + \frac{\partial (\rho uw)}{\partial x} + \frac{\partial (\rho vw)}{\partial y} + \frac{\partial (\rho w^2)}{\partial z} = -\frac{\partial p}{\partial z} + \frac{1}{Re}\left(\frac{\partial \tau_{xz}}{\partial x} + \frac{\partial \tau_{yz}}{\partial y} + \frac{\partial \tau_{zz}}{\partial z}\right). \tag{3.10}$$

4. Wing Geometry

The wing geometry and parameters used in the simulation are generally based on the Eviation Alice, an all-electric regional aircraft designed to carry nine passengers and two crew members and currently targeting an entry into service around 2027. Because the aircraft analyzed in this study shares a similar mission profile and operates in a comparable subsonic aerodynamic regime, the Eviation Alice is selected as the reference configuration.

The principal geometric parameters adapted from the Eviation Alice are the wingspan, root chord, and tip chord [15]. These provide a realistic basis for analyzing lift and induced drag under electric-aircraft operating conditions. The wing span of 18 m and a total wing planform area of 32.18 m^2 gives an aspect ratio of

$$AR = \frac{b^2}{S} = 10.068, \tag{4.1}$$

which is consistent with the relatively high-aspect-ratio wings considered for efficient subsonic aircraft, such as the Cessna Citation [16]. The wing has a taper ratio $\lambda = c_t/c_r = 0.5$ and a near-zero sweep angle (Λ_c) $\approx$ 0-5°, characteristic of high-aspect-ratio, low-sweep wings optimized for subsonic flight.

This model ensures that the computational simulations are representative of a practical, real-world electric aircraft wing. In addition to the baseline wing, various winglet designs were tested to analyze potential aerodynamic efficiency.

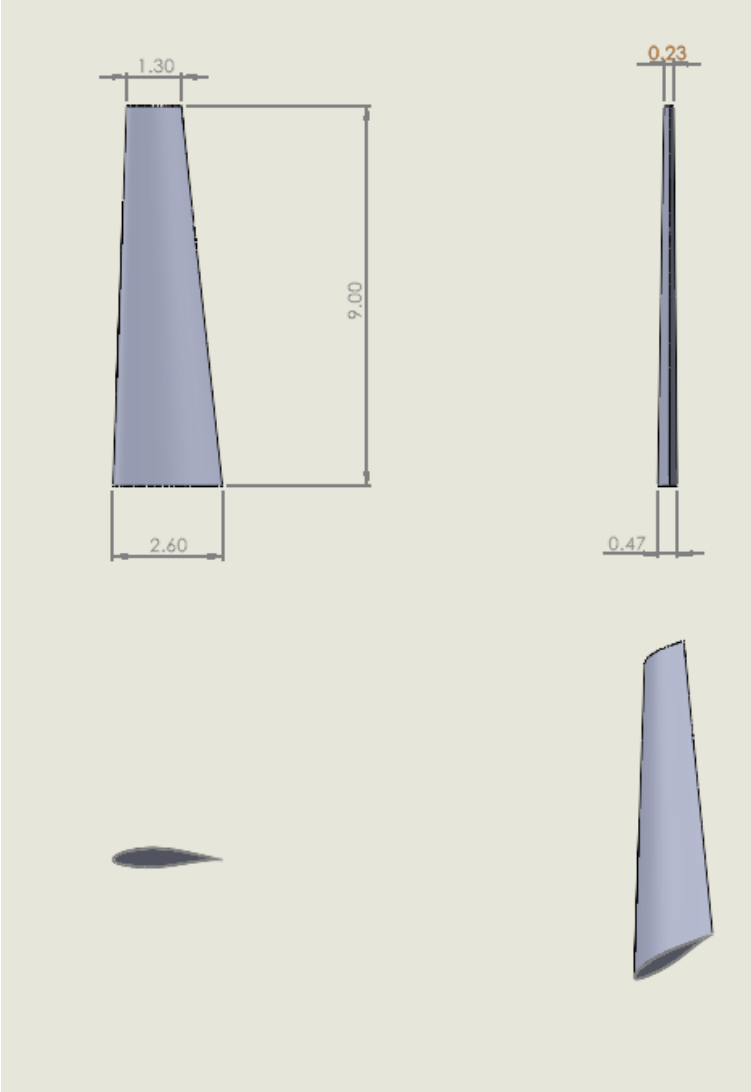


Figure 4.1: Wing geometry used in the simulations, showing the tapered, low-sweep planform and key dimensions (span, root chord, and tip chord).

4.1 NACA 63-418 Airfoil

NACA 63-418 is a laminar-flow airfoil designed to reduce skin-friction drag and achieve significantly lower section drag compared to conventional non-laminar [17]. The pressure distribution and thickness-to-chord profile are tailored to delay boundary-layer transition and minimize skin-friction drag. As a result, the airfoil sustains smooth, laminar flow over a large portion of both the upper and lower surfaces, which helps reduce viscous drag.

These characteristics make NACA 63-418 a strong candidate for electric aircraft that prioritize aerodynamic efficiency. The airfoil geometry also provides a favorable combination of design lift coefficient and thickness-to-chord ratio suitable for high-aspect-ratio, low-drag wings.

During preliminary airfoil selection, several alternative sections are also considered, including conventional NACA 4-series airfoils such as NACA 2412 and NACA 4412, as well as other

NACA 6-series laminar-flow sections (e.g., NACA 63-415). These candidates either exhibit higher profile drag at the target lift coefficient and Reynolds number or provide less favorable lift-to-drag characteristics for the intended cruise condition. For this reason, NACA 63-418 is selected as a strong candidate for an electric aircraft wing that prioritizes aerodynamic efficiency, offering a suitable combination of design lift coefficient and thickness-to-chord ratio for a highaspect-ratio, low-drag wing.

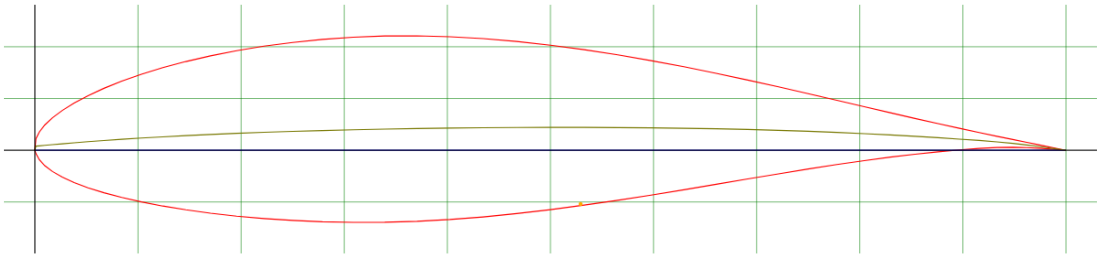


Figure 4.2: Geometry of the NACA 63-418 airfoil used for the wing, based on coordinates from AirfoilTools [18].

4.2 Geometry of 45-45 Conventional Winglet

The conventional winglet geometry is based on the winglet designs for contemporary regional and single aisle jets. To ensure that the aircraft would not have additional weight from larger winglets, a conventional winglet and a blended winglet are tested. The conventional winglet incorporates a cant angle and rearward sweep angle of 45° based off of covnentional winglet geometries. Its root chord matches the baseline-wing tip chord of 1.15 m, and the winglet tapers to a tip chord of approximately 0.54 m and has a vertical height of approximately 0.82 m. The winglet was tapered to a tip chord of approximately 0.54 m that would match with a taper ratio of 0.47.

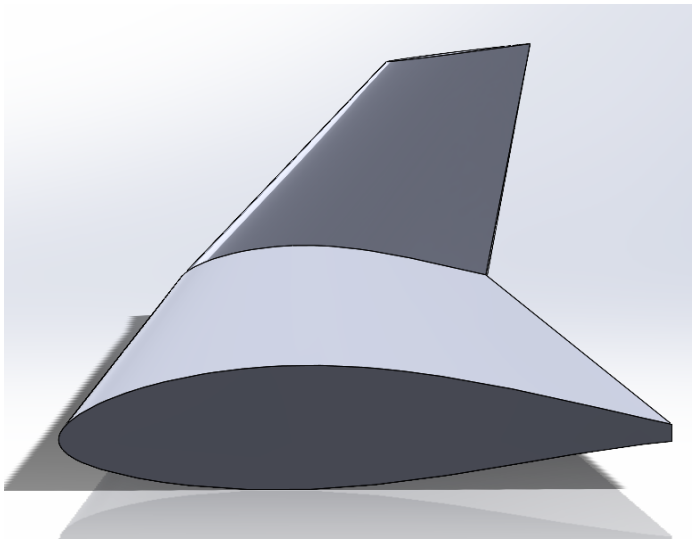


Figure 4.3: Isometric view of the conventional winglet configuration.

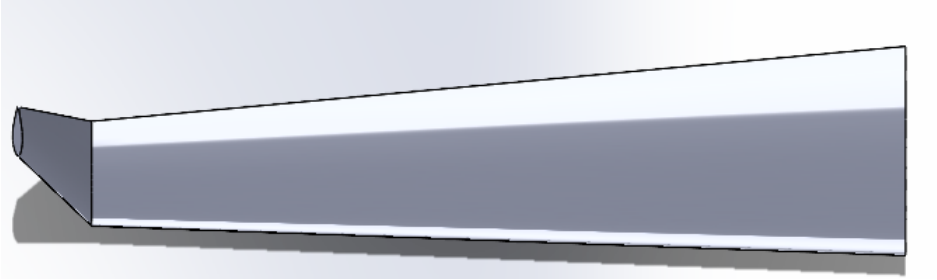


Figure 4.4: Top view of the conventional winglet configuration.

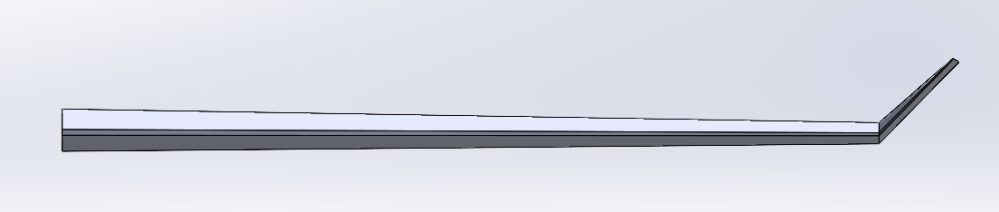


Figure 4.5: Side view of the conventional winglet configuration.

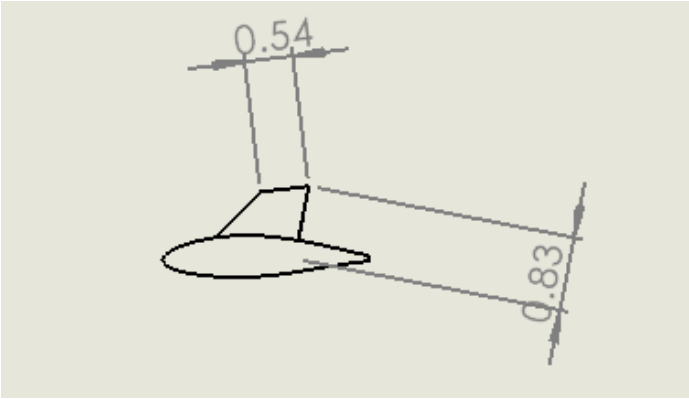


Figure 4.6: Head-on view showing the geometric dimensions of the conventional winglet.

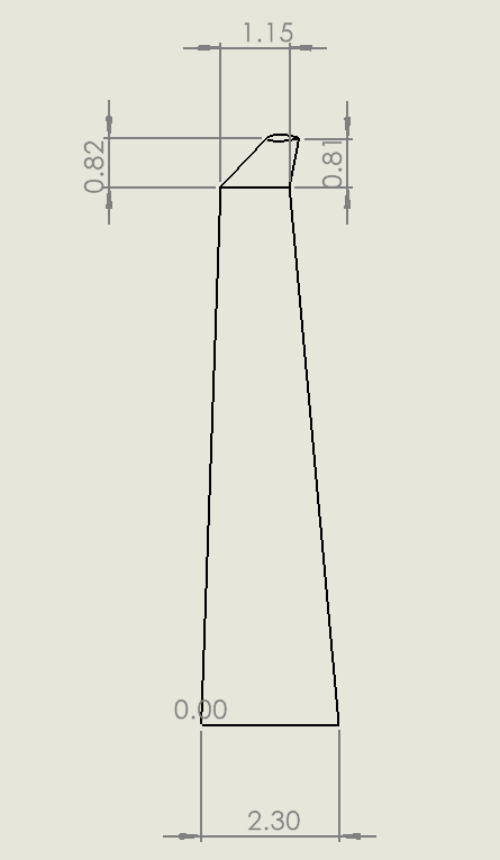


Figure 4.7: Top view showing the geometric dimensions of the conventional winglet.

4.3 Geometry of 45-45 Blended Winglet

The blended-winglet configuration incorporates a cant angle and sweep angle of 45°. While the conventional winglet's junction to the wing is an abrupt transition, the blended winglet use a smooth curved surface connecting the baseline wing to the winglet. The same cant and sweep angles are kept to leave a minimum difference in the orientation of the winglet. The goal of a smooth transition is to help increase the aerodynamic efficiency of the winglet by reducing any kind of interference at the junction. Blended winglets are commonly used on single-aisle aircraft such as the Boeing 737 Next Generation family. These designs use a smooth curved transition between the wing and winglet to reduce aerodynamic interference at the junction. Figure 4.7 presents the planform of the blended-winglet configuration.

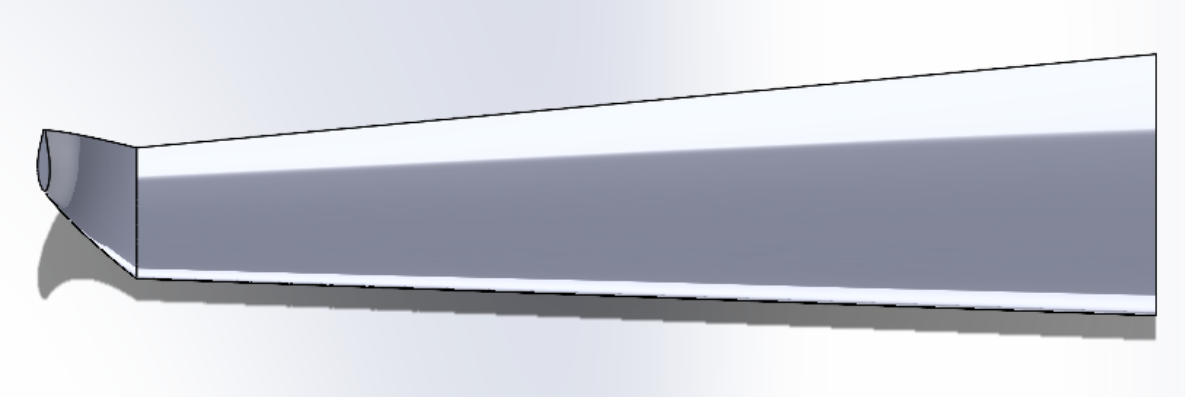


Figure 4.8: Top view of the 45-45 blended-winglet configuration.

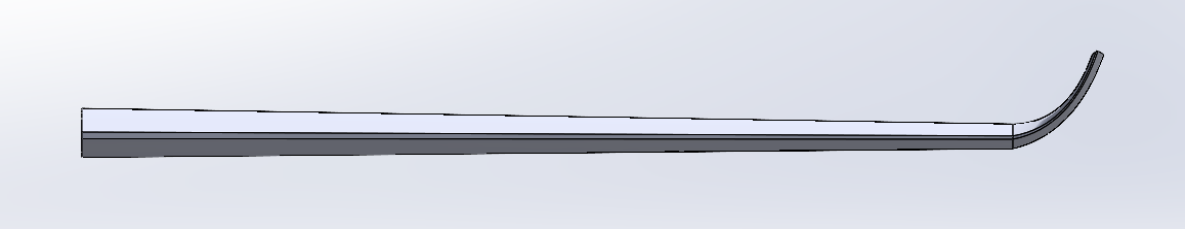


Figure 4.9: Side view of the 45-45 blended-winglet configuration.

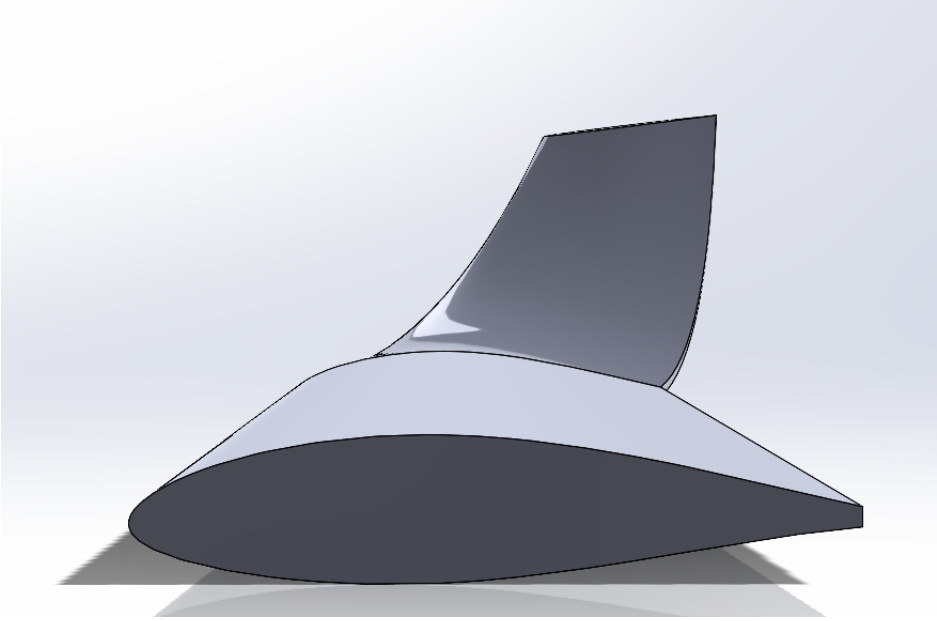


Figure 4.10: Isometric view of the 45-45 blended-winglet configuration.

5. Computational Domain and Boundary Conditions

The flow around the airfoil is modeled in a three-dimensional rectangular domain, as shown in Fig. X. Upstream distance is set to 5 meters, which is sufficient for the inflow velocity to stabilize before interacting with the leading edge of the wing. The downstream distance is extended in order to prevent the outlet boundary of the domain from impacting the flow at the trailing edge. Moreover, the vertical distances above and below the streamwise axis, which encompasses the vertical domain, are 5 meters. Furthermore, the box domain is extruded 12 meters to provide adequate domain for the half span of the wing, including the wingtips and the vortices generated. Overall, the airfoil is embedded in a large fluid block to provide ample space from the wing to the boundaries. The front face of the block is defined as the pressure-far-field inlet, the downstream face as the pressure outlet, and the remaining outer faces as far-field walls.

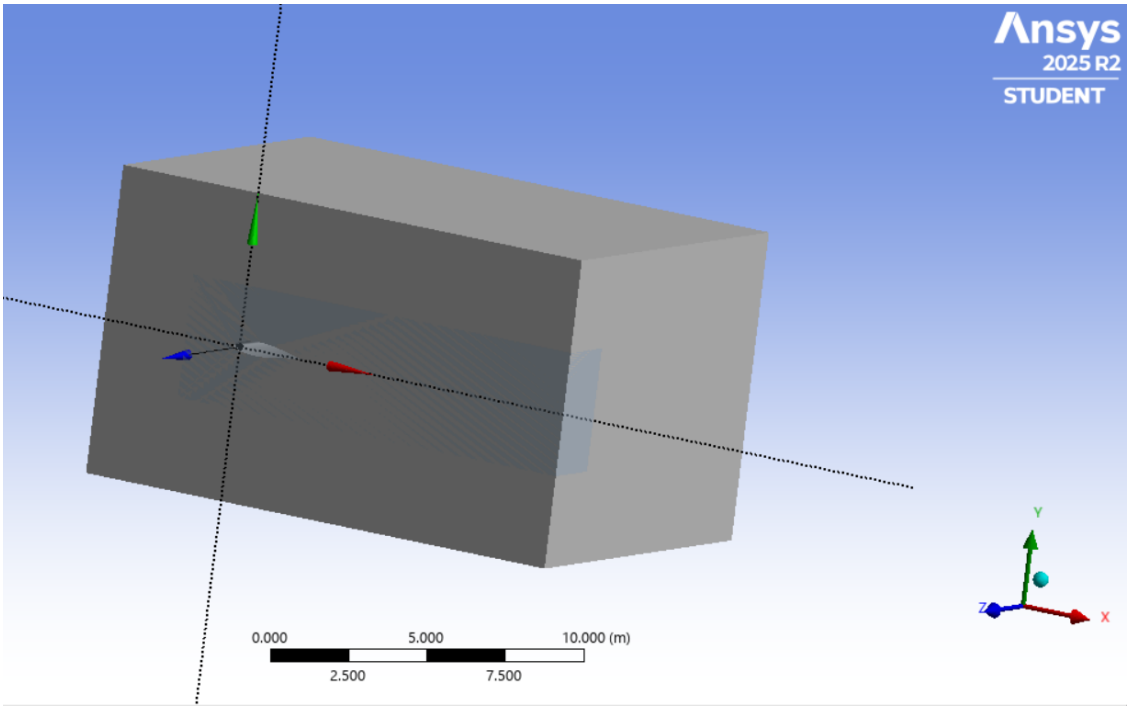


Figure 5.1: Sectional view of the computational domain showing the airfoil position relative to the global coordinate axes.

6. Mesh

The current mesh is created using a quadrilateral dominant mesh. The larger elements are in the far-field region in order to reduce computational cost, with finer elements located near the airfoil. Adaptive sizing is configurable, and global element size is set to the default value of 1.7869 m, a maximum element size of 3.5791 m, and a mesh growth rate of 1.3. The far-field region contains larger, coarser elements to reduce computational cost, and a progressive size reduction is implemented as the mesh approaches the airfoil surface. A face sizing with element sizing of 0.01 m is applied to refine the mesh on important surfaces such as the airfoil surface, inlets, and outlets. Inflation layers are applied to the airfoil surfaces to resolve the near-wall boundary layer. These settings produce very fine cells adjacent to the wall and a gradual increase in layer thickness away from the surface. A face sizing control is applied to the solid boundaries of the airfoil prescribing an element size of 0.01 m. This local refinement ensures that the surface geometry, particularly the leading and trailing edges of the airfoil, will have sufficient accuracy.

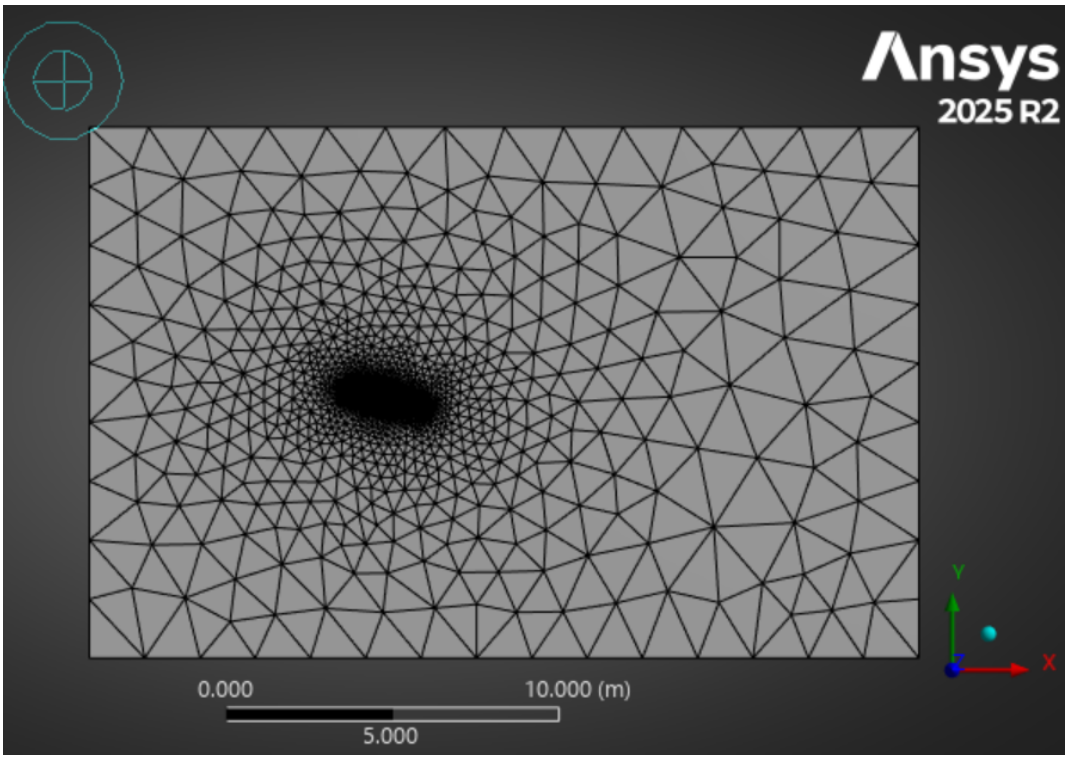


Figure 6.1: Finite element mesh generated in Ansys 2025 R2.

An unstructured surface mesh is generated around the wing using a quad-dominant meshing method. However, triangular elements are also generated, particularly around the curved wing surface and refined near-wall regions. Therefore, the final mesh is a quad-dominant unstructured mesh with triangular elements in complex regions. A higher mesh density is applied close to the wing surface. This local refinement is important because large velocity and pressure gradients are expected near the wall, especially within the boundary layer region. The mesh becomes gradually coarser away from the wing, where the flow gradients are smaller. This approach helps to reduce the total number of elements and maintain accuracy near the aerodynamic surface.

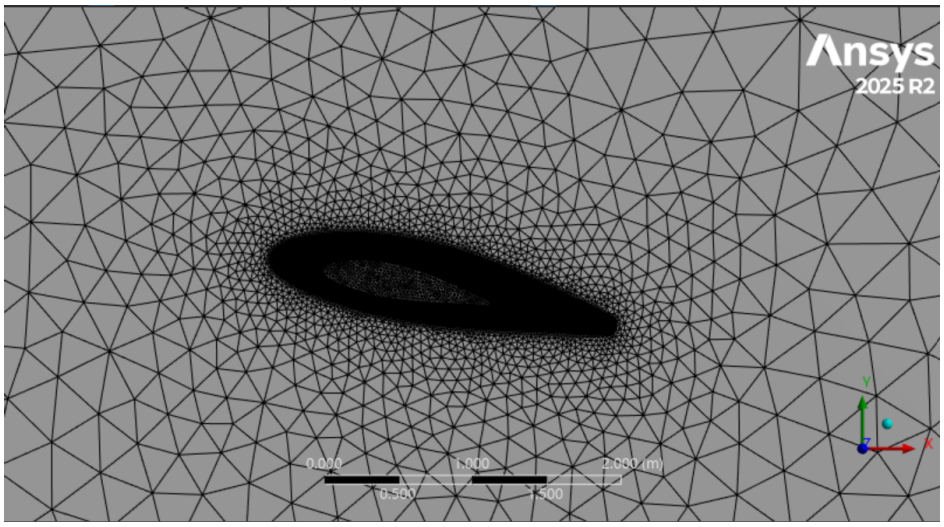


Figure 6.2: Computational mesh around the wing section.

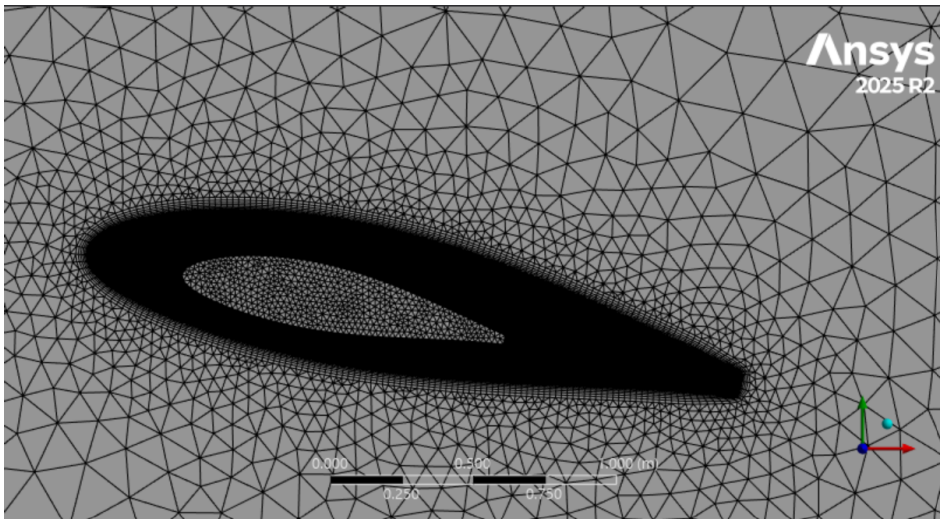


Figure 6.3: Refined computational mesh near the wing surface.

A quad-dominant unstructured meshing method is used; however, triangular elements are clearly visible in the refined region around the wing surface. The mesh density is highest near the leading edge, trailing edge, and wall region, where large pressure and velocity gradients are expected.

The fine mesh around the wing improves the accuracy of pressure, lift, drag, and wall shear stress. Away from the wing, the mesh becomes gradually coarser because the flow gradients are smaller in the far-field region. This mesh arrangement provides a balance between computational cost and solution accuracy.

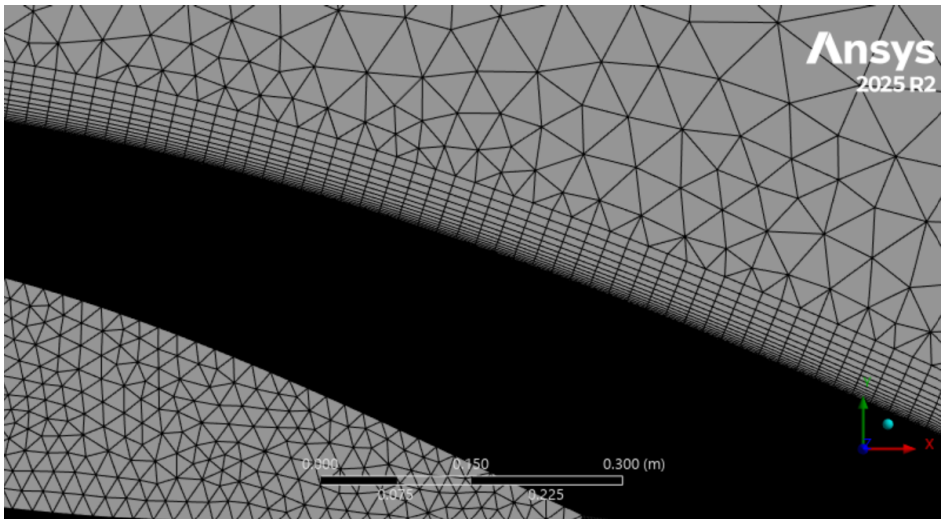


Figure 6.4: Inflation layers near the wing surface.

Inflation layers are applied close to the wing wall to improve the resolution of the boundary layer. A total of 15 inflation layers are applied near the wing surface, with a first layer height of 1.0×10^{-3} m and a growth rate of 1.18. These structured layers allow the velocity gradient near the wall to be captured more accurately, which is important for predicting wall shear stress and drag.

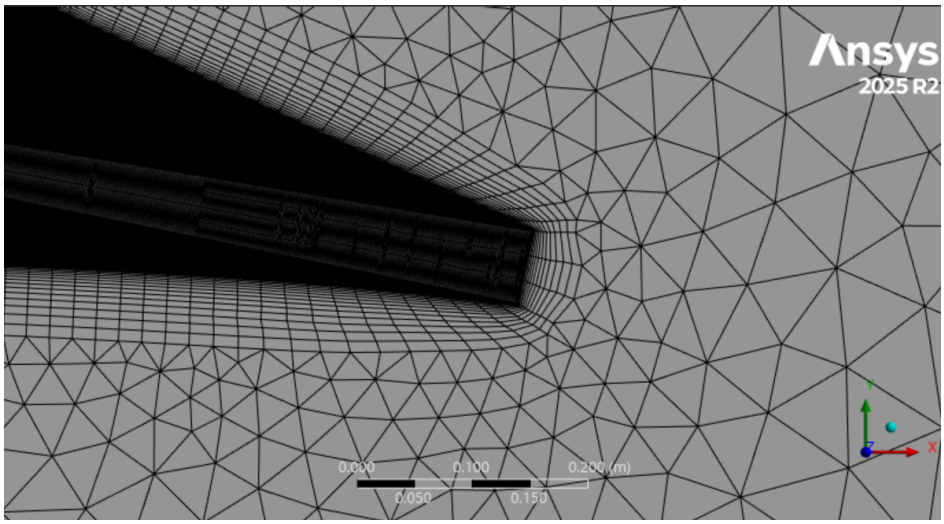


Figure 6.5: Close-up view of the inflation layers near the wing trailing edge.

At the trailing-edge of the wing, a maximum of 15 inflation layers is used, with a first layer height of 1.0×10^{-3} m and a growth rate of 1.18. The inflation mesh gradually transitions into the surrounding unstructured triangular mesh away from the wall. This mesh strategy improves the accuracy of wall shear stress and drag prediction and maintains a reasonable computational cost. For the blended-winglet configuration at 10° angle of attack, the inflation is reduced to 12 inflation layers and a growth rate is adjusted to 1.15 due to computational costs.

7. Results

7.1 Baseline Configuration at 0° Angle of Attack

Table 7.1: Aerodynamic coefficients for the baseline configuration at 0° angle of attack.

Coefficient	**Value**
Lift coefficient, C_L	0.14519
Drag coefficient, C_D	0.014293
Lift-to-drag ratio, L/D	10.158

The aerodynamic coefficients obtained for the baseline wing configuration at 0° angle of attack, included the final converged solution that produced a lift coefficient of $C_L = 0.14519$ and a drag coefficient of $C_D = 0.014293$, resulting in a lift-to-drag ratio of approximately $L/D = 10.158$. Ansys Fluent identified the solution as converged at iteration 95.

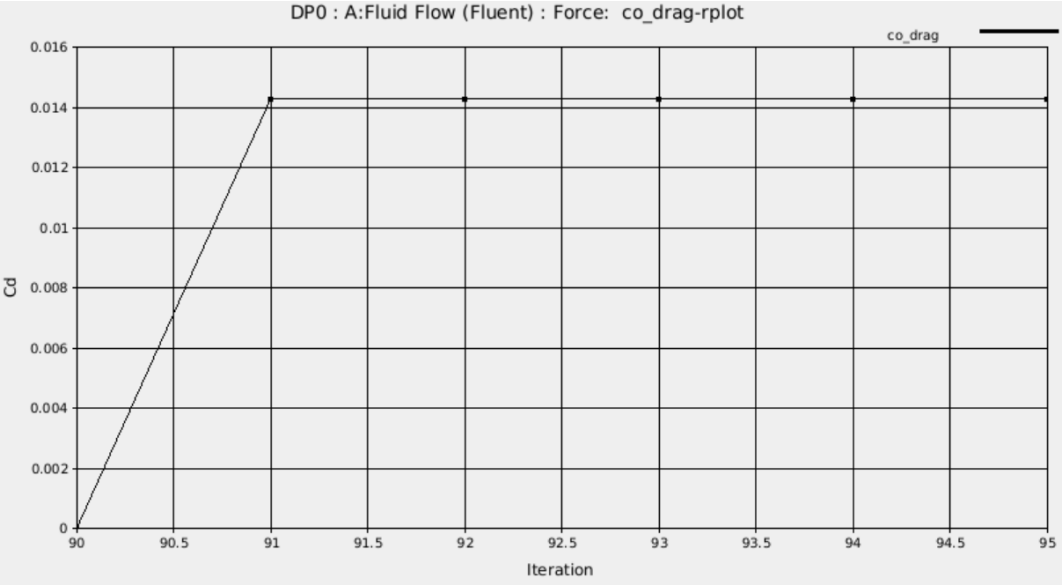


Figure 7.1: Coefficient of drag convergence plot at 0° angle of attack for the baseline configuration.

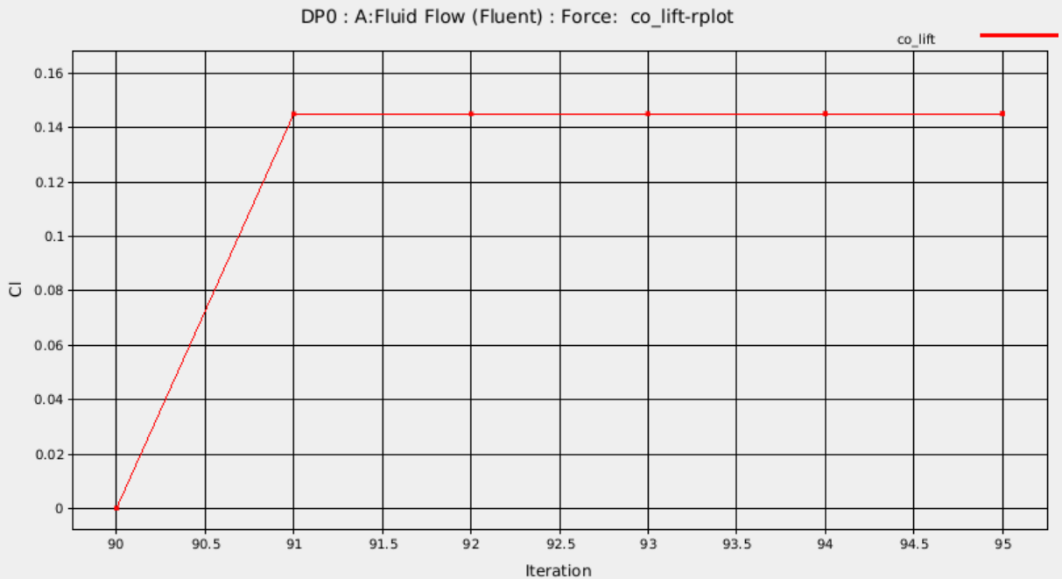


Figure 7.2: Coefficient of lift convergence plot at 0° angle of attack for the baseline configuration.

The wall shear stress ranged from 0.26 Pa to 73.35 Pa. The highest wall shear stress was observed close to the leading-edge region, where the incoming flow first interacted with the wing surface. Moving downstream along the chord, the wall shear stress gradually decreased.

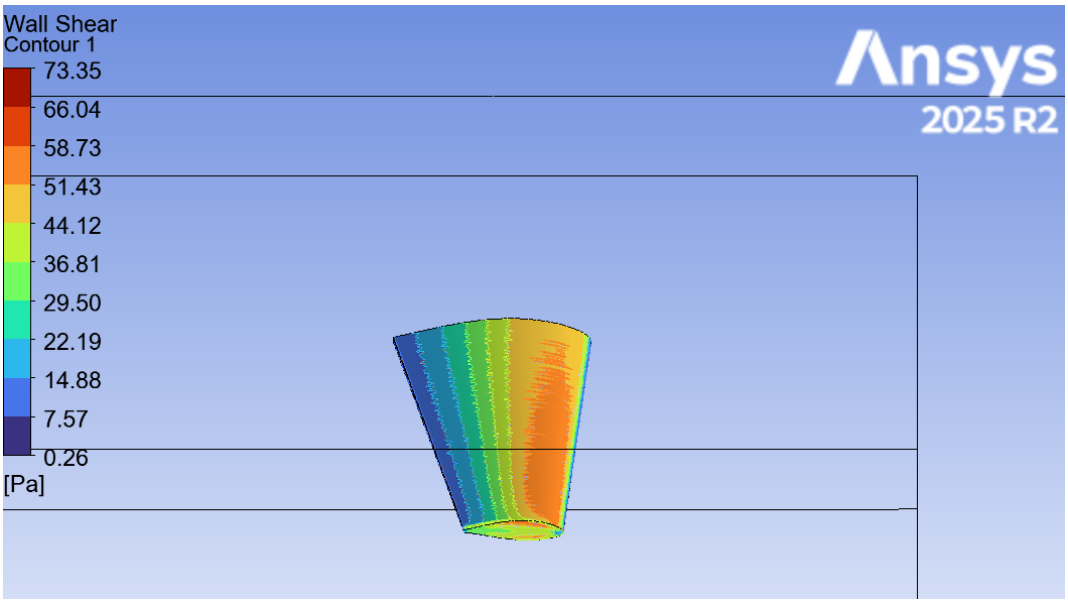


Figure 7.3: Wall shear contour at 0° angle of attack for the baseline configuration.

The pressure for zero angle of attack varied between approximately -1.606×10^4 Pa and 1.170×10^4 Pa.

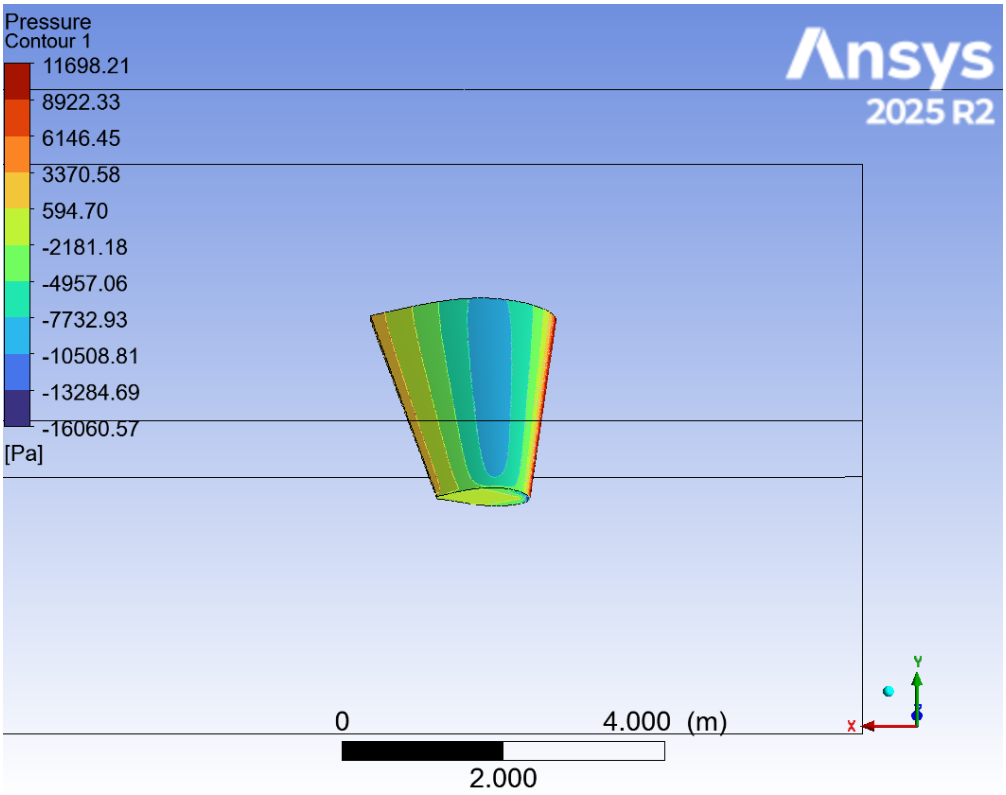


Figure 7.4: Pressure contour at 0° angle of attack for the baseline configuration.

The contour indicated that the pressure was distributed relatively smoothly over the wing surface, with higher pressure regions occurring near the leading-edge area where the incoming flow first met the wing. At zero angle of attack, the pressure difference between the upper and lower surfaces was expected to be relatively small compared with higher angle-of-attack cases.

At 0° angle of attack, a concentrated vortex structure formed near the wingtip and extended downstream into the wake. The visible structure remained relatively localized close to the wingtip, which matched the lower aerodynamic loading at this angle of attack. The simulations measured the vortex swirling strength. In this simulation, a value of 0-50 s^{-1} was chosen for all configurations and angles of attack, which was to maintain a consistent colors scale across all cases. This allowed a proper comparison with other wing configurations. Values near 50 s^{-1} indicated strong rotation flow that demonstrates a weaker rotation in the wake.

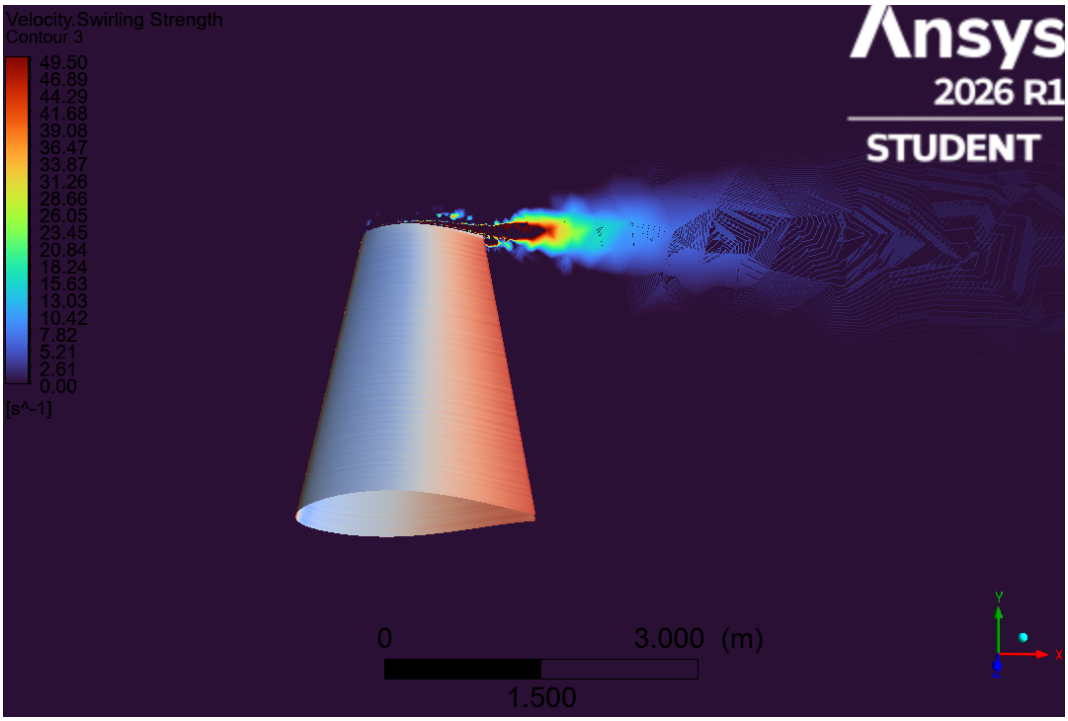


Figure 7.5: Swirling-strength contour of the near-tip wake for the baseline-wing configuration at 0° angle of attack.

As seen in the contour, the higher values were concentrated in the areas closer to the wingtip, and the voriticity faded away downstream. This was generally consistent with low aerodynamic efficiency, in which the baseline wing at 0° experienced L/D of 10.158.

7.2 Baseline Configuration at 6° Angle of Attack

The lift and drag coefficient produced for the baseline wing at 6° angle of attack was coefficient of $C_L = 0.72537$ and a coefficient of $C_D = 0.033054$, respectively. As a result, the lift-to-drag ratio was approximately $L/D = 21.945$. Ansys Fluent identified the solution as converged at iteration 85.

Table 7.2: Aerodynamic coefficients for the baseline configuration at 6° angle of attack.

Coefficient	**Value**
Lift coefficient, C_L	0.72537
Drag coefficient, C_D	0.033054
Lift-to-drag ratio, L/D	21.945

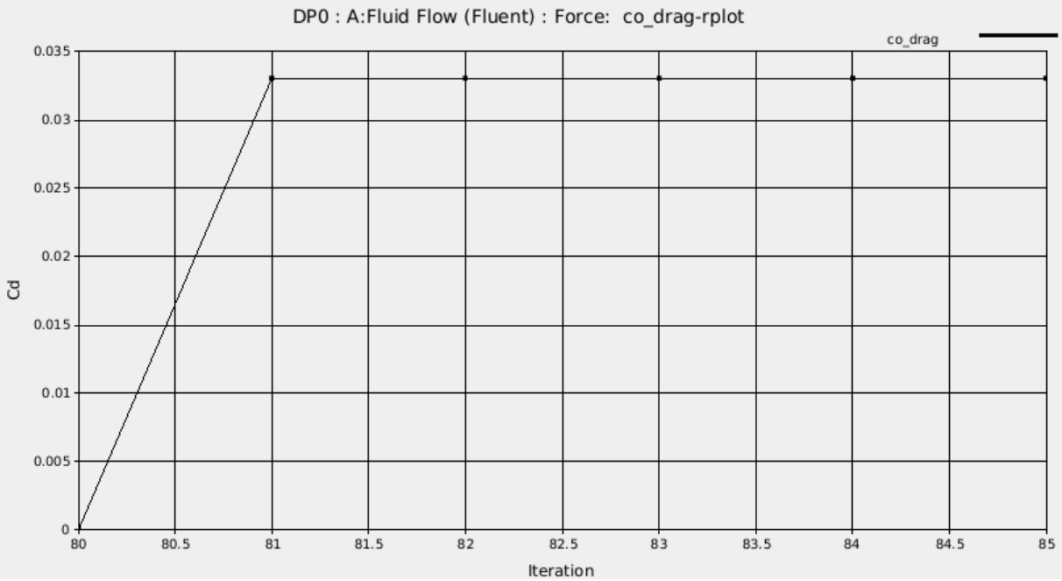


Figure 7.6: Coefficient of drag convergence plot at 6° angle of attack for the baseline configuration.

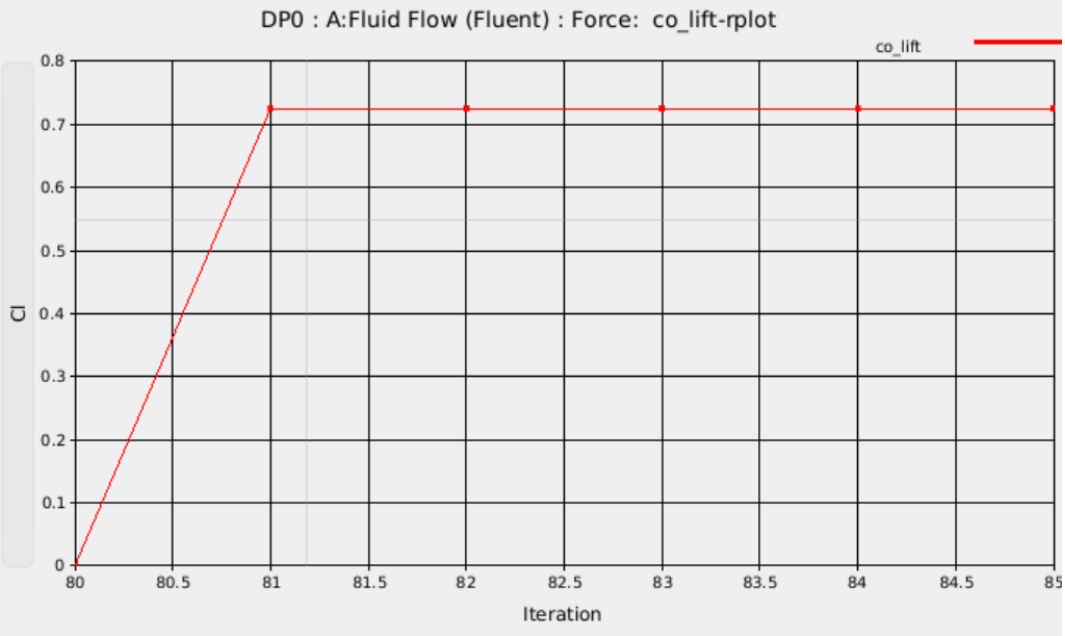


Figure 7.7: Coefficient of lift convergence plot at 6° angle of attack for the baseline configuration with the new reference area.

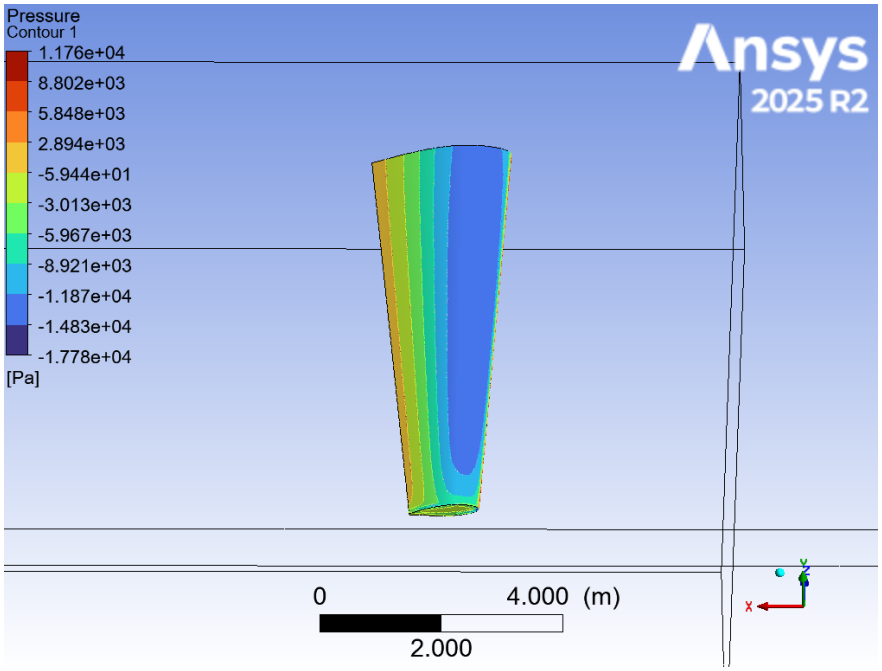


Figure 7.8: Pressure contour at 6° angle of attack for the baseline configuration.

As shown in Figure 7.8, the pressure at 6° ranged from -1.778×10^4 Pa to 1.176×10^4 Pa. The maximum pressure remained mostly unchanged, increasing only from 1.169821×10^4 Pa to 1.176×10^4 Pa. However, the minimum pressure became much less, decreasing from -1.606×10^4 Pa at 0° to -1.778×10^4 Pa at 6°. This was an increase of 10.7% in terms of minimum pressure.

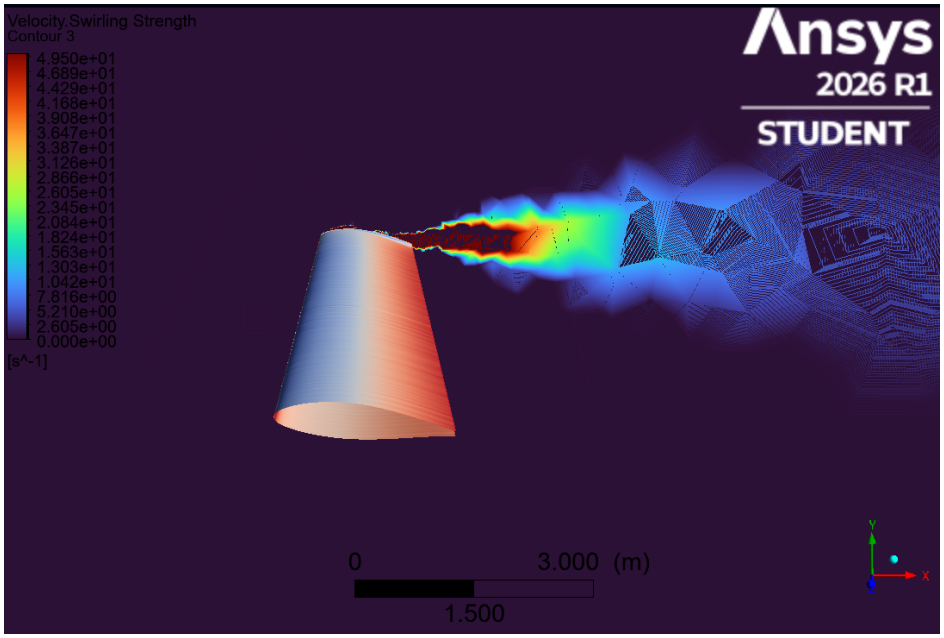


Figure 7.9: Swirling-strength contour of the near-tip wake for the baseline-wing configuration at 6° angle of attack.

The wingtip vortex structure at the tip of the baseline wingtip was larger and stretched more farther downstream. This correlated with the higher angle of attack that was being simulated.

This was generally consistent with the the change in aerodynamic coefficients, as C_L increased significantly more than C_D. The change in C_L overcame the change in C_D, generating a much higher L/D.

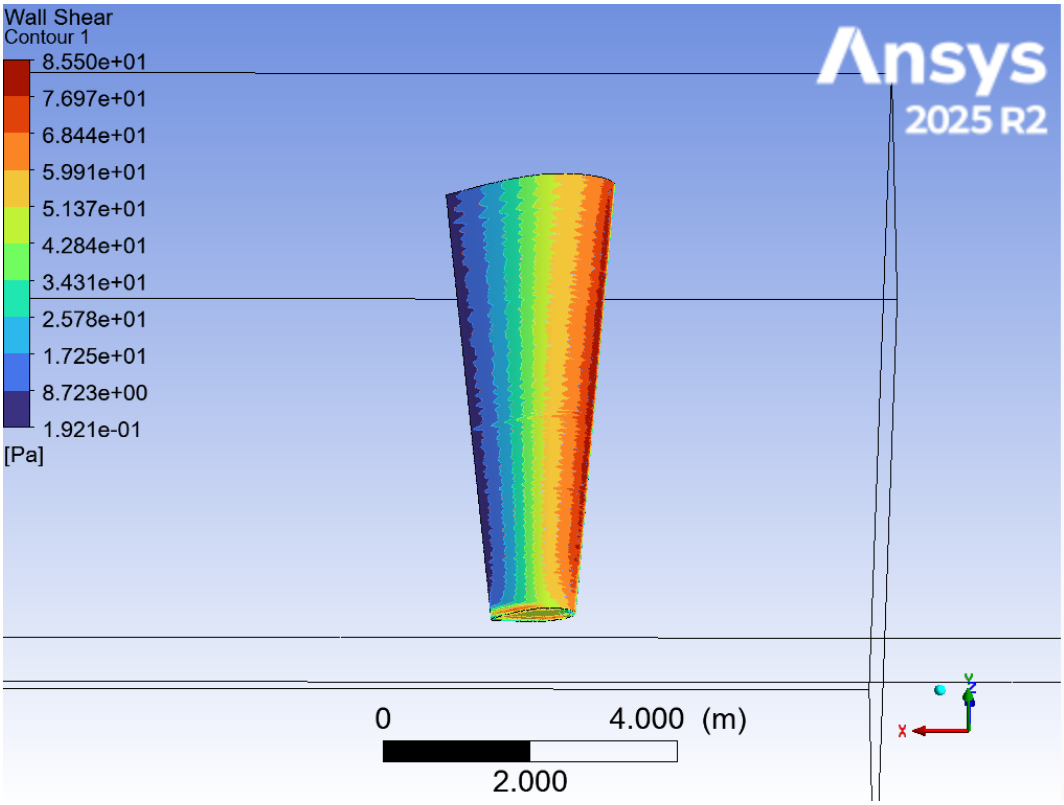


Figure 7.10: Wall shear contour at 6° angle of attack for the baseline configuration with the new reference area.

The wall shear stress for 6° for baseline wing varied from approximately 0.1972 Pa to 85.49 Pa. In comparison to the 0° angle of attack, the wall shear stress increased from approximately from 73.35 Pa to 85.5 Pa, an increase of approximately 16.6%. Higher wall shear stress was observed near the leading-edge region, where the incoming flow first interacted with the wing surface and the velocity gradient close to the wall was relatively large.

7.3 Baseline Configuration at 10° Angle of Attack

The converged solution for 10° angle of attack of baseline wing produced a lift coefficient of $C_L = 1.0719$ and a drag coefficient of $C_D = 0.058153$, resulting in a lift-to-drag ratio of approximately $L/D = 18.432$. Ansys Fluent identified the solution as converged at iteration 75, and the relatively high lift coefficient was consistent with the increased angle of attack.

Table 7.3: Aerodynamic coefficients for the baseline configuration at 10° angle of attack.

Coefficient	**Value**
Lift coefficient, C_L	1.0719
Drag coefficient, C_D	0.058153
Lift-to-drag ratio, L/D	18.432

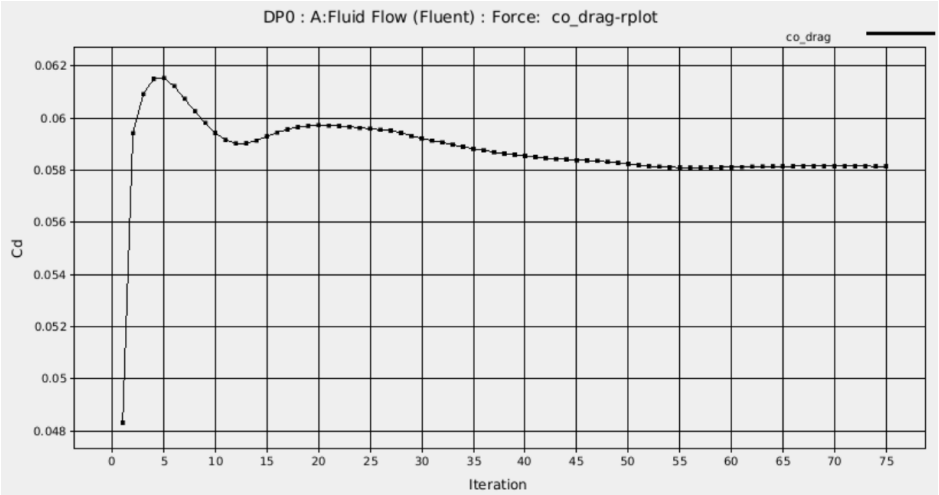


Figure 7.11: Drag-coefficient convergence history for the baseline wing configuration at 10° angle of attack.

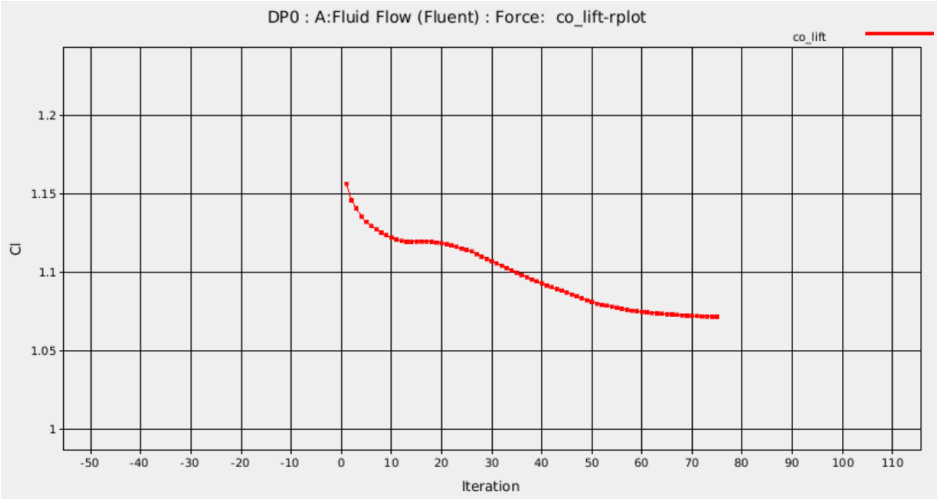


Figure 7.12: Lift-coefficient convergence history for the baseline wing configuration at 10° angle of attack.

The pressure distribution over the baseline wing at an angle of attack of 10° was greatest at the leading edge and least at the trailing edge. Compared to 0° and 6°, the maximum pressure

increased only slightly but the minimum pressure decreased significantly more, decreasing from -1.778×10^4 Pa at 6° to -2.672×10^4 Pa at 10°. This demonstrated a greater pressure difference than other angles of attack, which indicated more lift and drag.

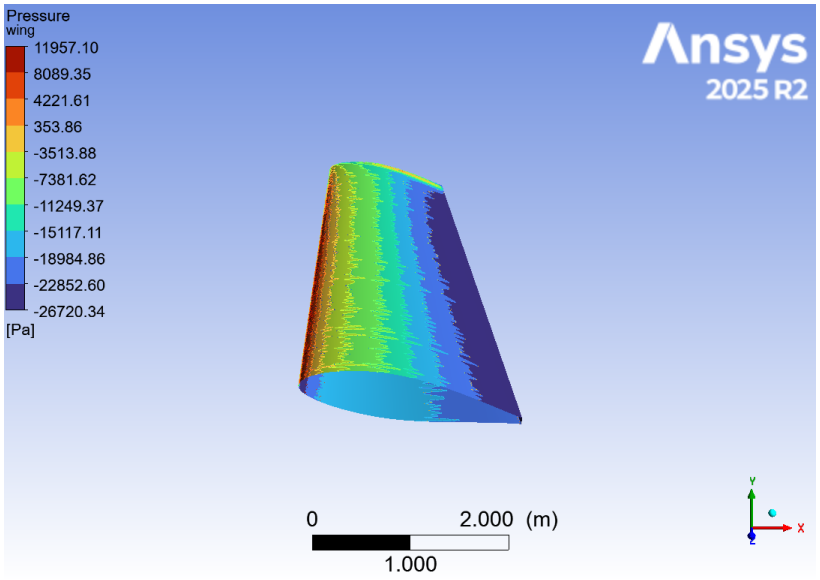


Figure 7.13: Pressure distribution over the baseline wing configuration at 10° angle of attack.

The wall shear stress at 10° angle of attack ranged from 0.11 Pa to 123.54 Pa. Similar to 0° and 6°, the highest wall shear stress was at the leading edge and decreased toward the trailing edge.

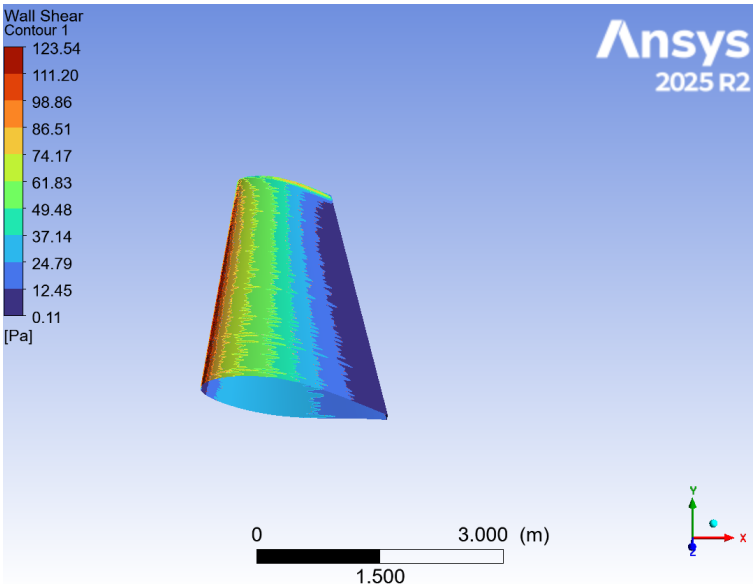


Figure 7.14: Wall-shear-stress distribution over the baseline wing configuration at 10° angle of attack.

In contrast, the magnitude of the the shear stress was significantly higher at 10° compared to 0° and 6°. The higher maximum wall shear stress at 10°, compared to the other cases, indicating

stronger local viscous effects and helped explain the increase in drag. This demonstrated that the additional lift generated at 10° was correlated to a greater drag increase.

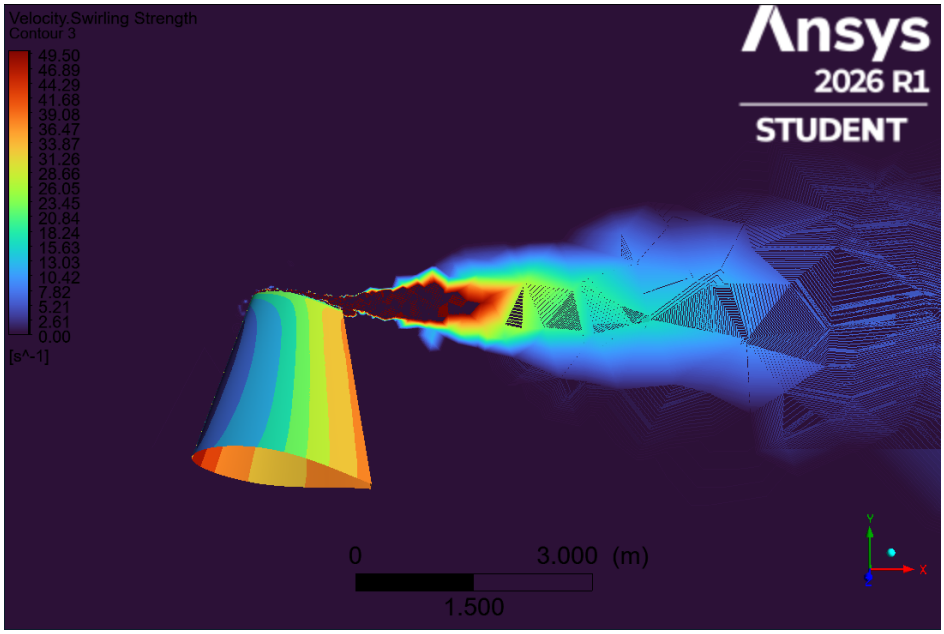


Figure 7.15: Swirling-strength contour of the near-tip wake for the baseline-wing configuration at 10° angle of attack.

The swirling strength at 10° for the baseline wing had a more developed wake than the baseline wing at 6°. This was consistent with an increase in C_D, indicating downstream wake development. This contributed to loss of aerodynamic efficiency, as noted in L/D.

7.4 45-45 Winglet Configuration at 0° Angle of Attack

The converged solution for the 45-45 blended-winglet configuration at 6° angle of attack using the coarser mesh produced a lift coefficient of $C_L = 0.74098$ and a drag coefficient of $C_D = 0.037906$, resulting in a lift-to-drag ratio of approximately $L/D = 19.548$. The relatively high lift coefficient was consistent with the increased angle of attack, and the lift-to-drag ratio indicated that the configuration maintained favorable aerodynamic efficiency at 6°.

Table 7.4: Aerodynamic coefficients for the conventional non-blended winglet configuration with a 45° cant angle and 45° sweep angle at 0° angle of attack.

Coefficient	**Value**
Lift coefficient, C_L	0.15260
Drag coefficient, C_D	0.014989
Lift-to-drag ratio, L/D	10.181

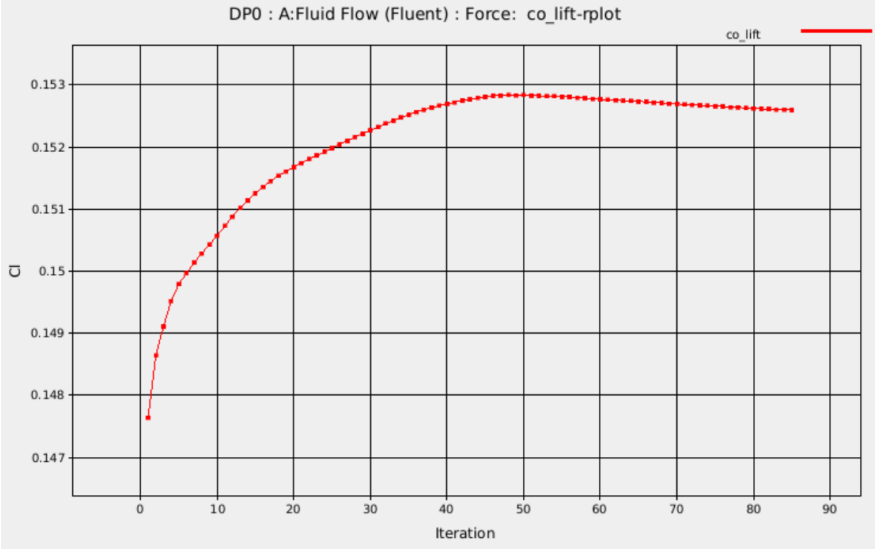


Figure 7.16: Lift-coefficient convergence history for the 45-45 winglet configuration at 0° angle of attack.

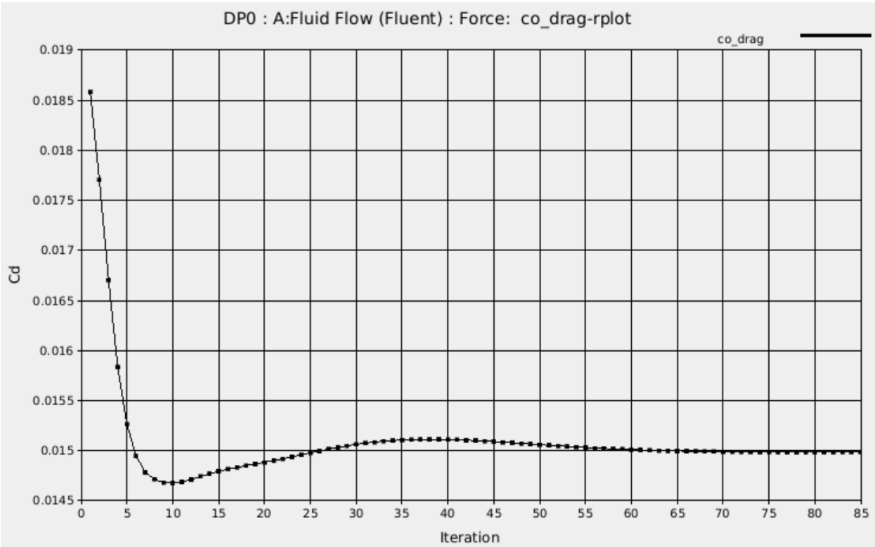


Figure 7.17: Drag-coefficient convergence history for the 45-45 winglet configuration at 0° angle of attack.

At 0° angle of attack, the conventional winglet demonstrated similar wall shear stress ranges, as shown in Figure 7.18. The conventional winglet produced a lower maximum wall shear stress of 62.7 Pa, compared with 73.35 Pa for the baseline wing. This reduction may have been due to how the winglet affected the flow near the wall near the surface and cause a difference in the boundary-layer behavior.

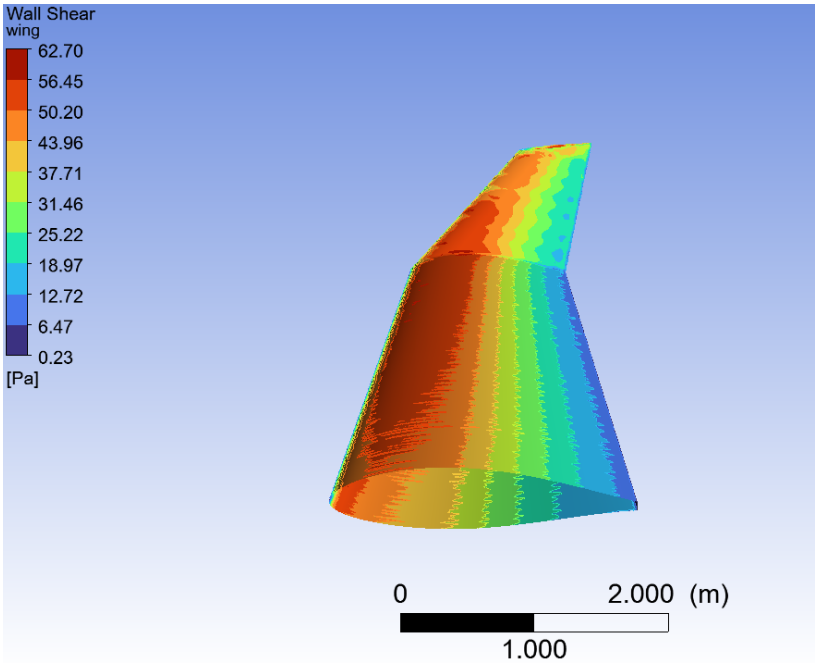


Figure 7.18: Wall shear stress distribution for the conventional winglet configuration at 0° angle of attack.

In the pressure contour of the conventional winglet at 0°, the pressure ranged from approximately -8.95×10^3 Pa to 1.17×10^4 Pa. This contrasts with the minimum pressure of the baseline-wing configuration at 0°, whose magnitude was approximately 56.9% lower than that of the conventional-winglet.

Figure 7.19 visualizes the highest pressure at the leading edge and the pressure decreasing toward the trailing edge and towards the winglet, indicating that the winglet appeared to change the aerodynamic loading near the wingtip. The maximum pressure of this winglet was only 0.17% lower than the baseline value, leaving the maximum pressures mostly unchanged. Due to the significantly lower minimum pressure that the conventional wing exhibited, the increase in lift was most likely due to the overall pressure and the loading of the wing and winglet instead of an increase in suction.

The conventional winglet produced a more compact vortex close to the tip of the winglet, as shown in Figure 7.20. The wake originated from the outer tip of the winglet. The wake appeared to decay over a shorter distance, demonstrating that the winglet had an effect on the distribution of the wake. While the wake became more compact in size, the drag coefficient only increased slightly. Although both coefficients increased, C_L increased proportionally slightly more than C_D, causing L/D to increase marginally. This suggested that the winglet had a smaller effect on the aerodynamic efficiency at 0° of the conventional winglet configuration.

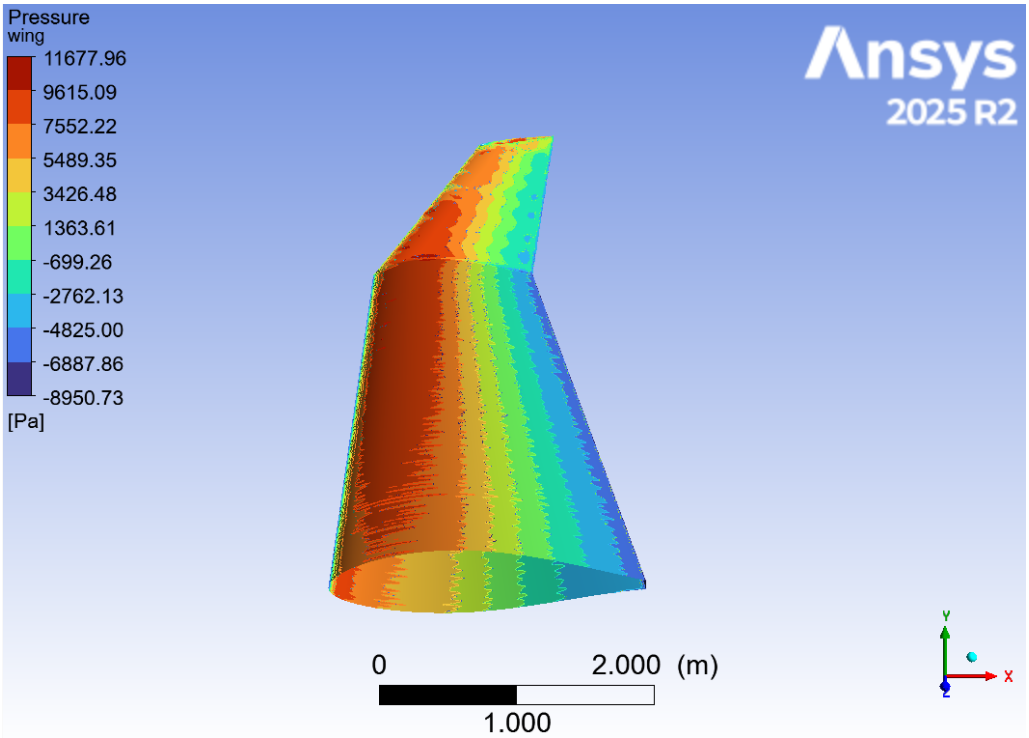


Figure 7.19: Pressure contour at 0° angle of attack for the 45-45 winglet configuration.

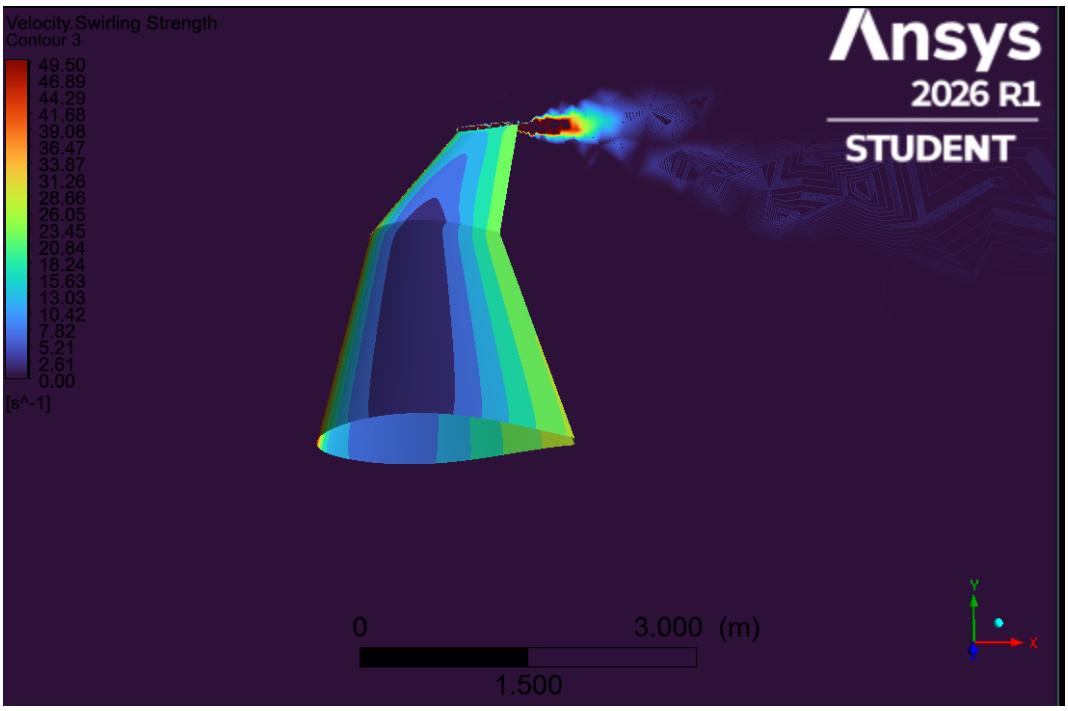


Figure 7.20: Swirling-strength contour of the near-tip wake for the conventional-winglet configuration at 0° angle of attack.

7.5 45-45 Winglet Configuration at 6° Angle of Attack

The lift coefficient for the 45-45 winglet configuration at 6° was $C_L = 0.78168$, and the drag coefficient was $C_D = 0.033105$. The resulting lift-to-drag ratio was $L/D = 23.612$, indicating that the configuration achieved greater aerodynamic efficiency at 6° than both the baseline wing at 6° and the conventional winglet configuration at 0°. In comparison to the 6° of the baseline wing, the lift-to-drag ratio of the wing equipped with the conventional winglet improved by 7.6%, increasing aerodynamic efficiency. Compared with the 0°, angle-of-attack case, both lift and drag increased, which was expected because increasing the angle of attack strengthened the pressure difference between the upper and lower surfaces of the wing.

Table 7.5: Aerodynamic coefficients for the 45-45 winglet configuration at 6° angle of attack.

Coefficient	**Value**
Lift coefficient, C_L	0.78168
Drag coefficient, C_D	0.033105
Lift-to-drag ratio, L/D	23.612

The maximum wall shear stress of the conventional winglet increased slightly from 85.5 Pa to 85.98 Pa of the baseline wing at 0°. However, the difference of the minimum wall shear stress was 27.1%, decreasing from 0.1921 Pa to 0.14 Pa.

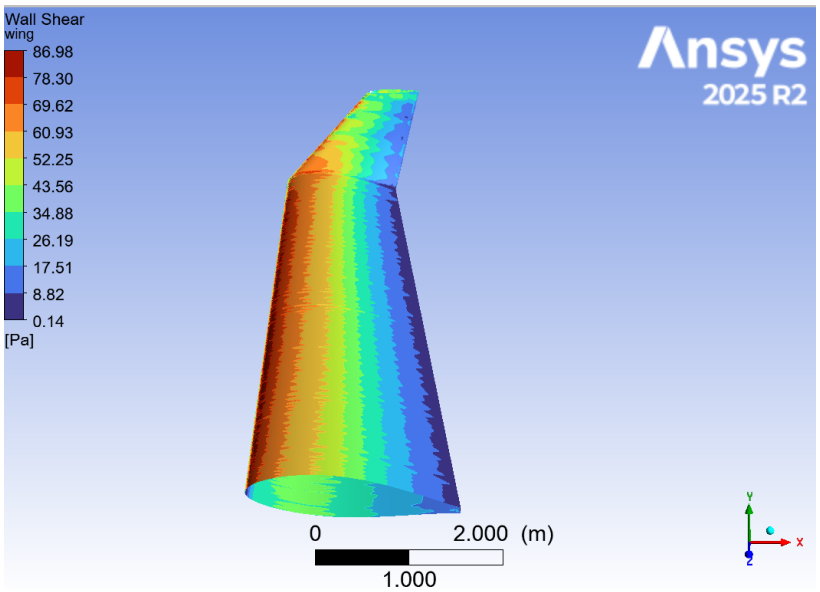


Figure 7.21: Wall shear stress contour at 6° angle of attack for the 45-45 winglet configuration.

The maximum wall sear stress remained nearly unchanged between the baseline and conventional-winglet configuarions, indicating that the near-wall velocity gradient was similar for both configurations. The minimum values for both configurations were close to zero, indicating locally reduced flow momentum and greater flow speration.

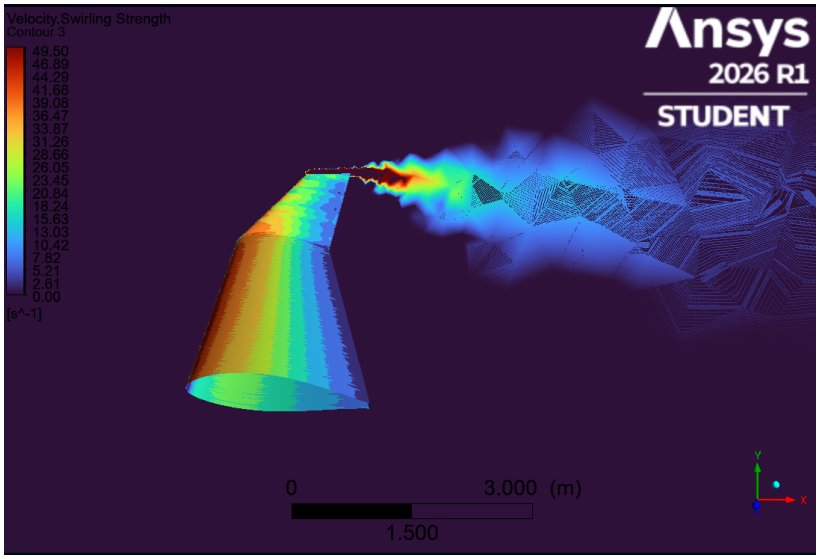


Figure 7.22: Swirling-strength contour of the near-tip wake for the conventional-winglet configuration at 6° angle of attack.

In comparison to the 6° baseline wing, the wake at the winglet of the conventional configuration at 6° was relatively more concentrated to the winglet tip. The higher swirling strength regions of the conventional configuration appeared smaller than that of the baseline wing. The conventional winglet had a more concentrated high-Q region near the winglet tip than the baseline wing. While its total drag coefficient increased slightly, the winglet generated a greater amount of lift, leading to an improvement of the L/D ratio. As a result, the higher L/D ratio was due to more lift that was generated rather than the decrease in wake size, since C_D only increased very marginally.

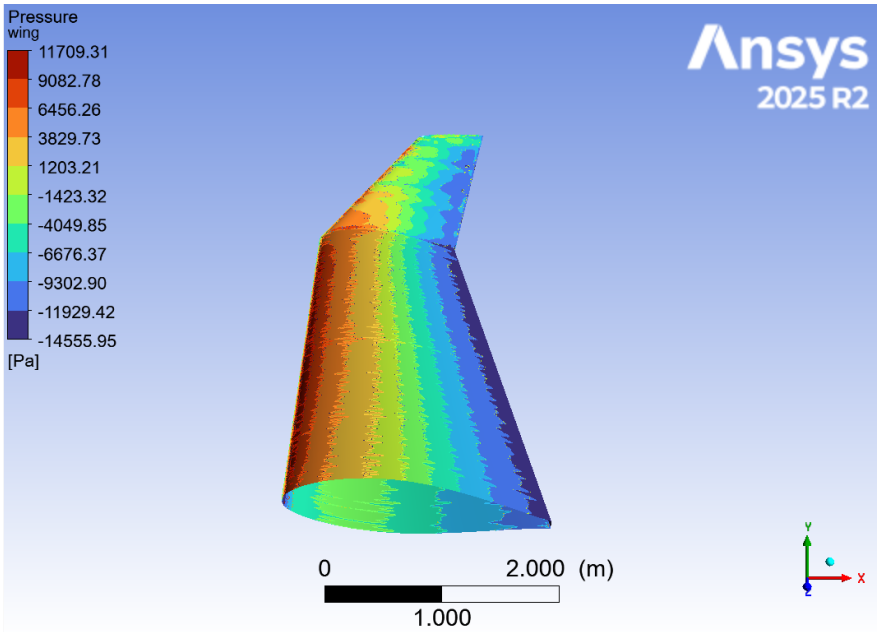


Figure 7.23: Pressure contour at 6° angle of attack for the 45-45 winglet configuration.

At 6° angle of attack for the conventional winglet, the pressure ranged from -1.46×10^4 Pa to 1.17×10^4 Pa. Compared with the baseline configuration, the maximum pressure decreased by 0.43%. The magnitude of the minimum pressure decreased by 18.1%. In comparison to the baseline configuration at 0°, C_L increased by about 7.8%, and C_D increased by only 0.15%. Despite the conventional winglet having a weaker suction, it produced a higher C_L. This was most likely attributed to changes in the pressure across both the wing and the winglet.

7.6 45-45 Winglet Configuration at 10° Angle of Attack

The conventional winglet at 10° had an increase in lift-to-drag ratio by about 6.08% in comparison to 6°. The Cl increased from 1.0717 to 1.1414, and Cd incrementally increased from 0.058153 to 0.058377. The lift to drag ratio for the conventional winglet at 10° decreased by 17.2% from 6° to 10°, indicating less aerodynamic efficency at 10°, despite more lift generated.

Table 7.6: Aerodynamic coefficients for the 45-45 winglet configuration at 10° angle of attack.

Coefficient	**Value**
Lift coefficient, C_L	1.1414
Drag coefficient, C_D	0.058377
Lift-to-drag ratio, L/D	19.552

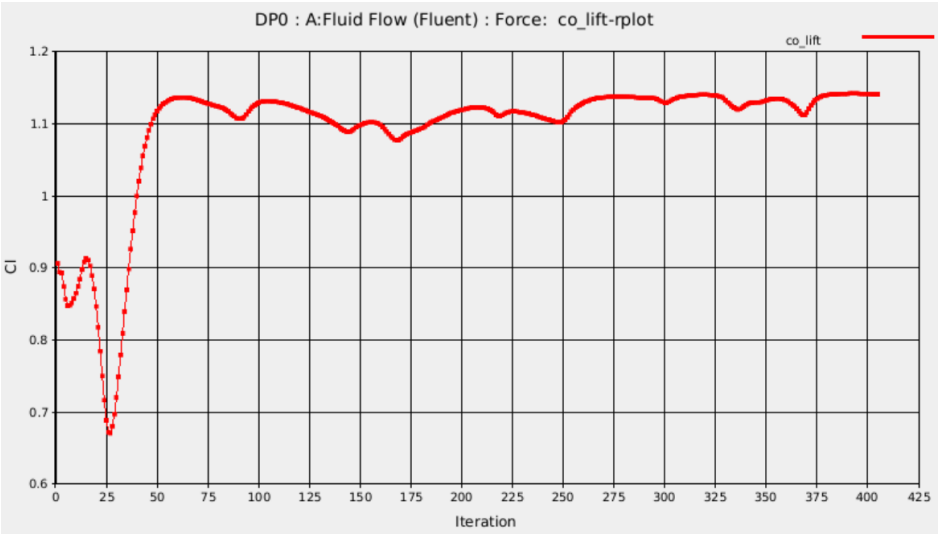


Figure 7.24: Lift-coefficient iteration history for the 45-45 winglet configuration at 10° angle of attack.

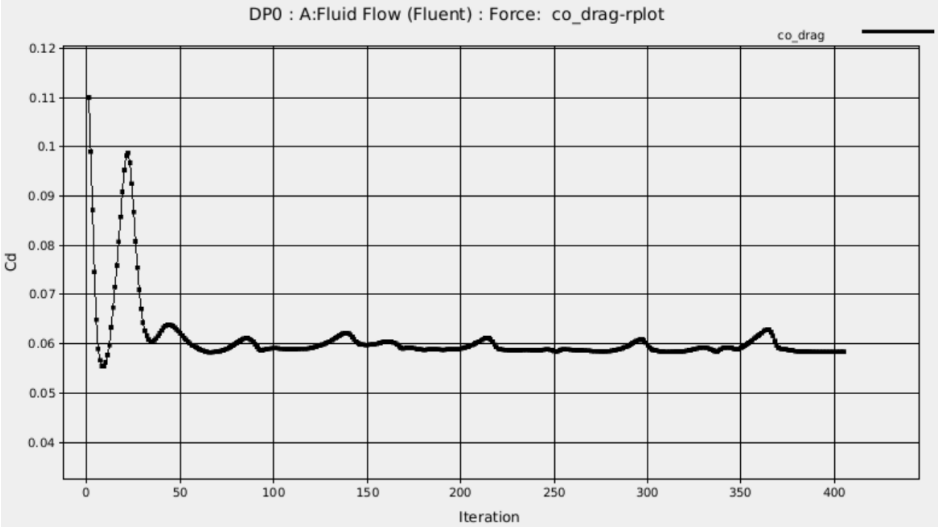


Figure 7.25: Drag-coefficient iteration history for the 45-45 winglet configuration at 10° angle of attack.

As shown in Figure 7.26, the pressure for the winglet at 10° ranged from -2.74×10^4 Pa to 1.19×10^4 Pa.

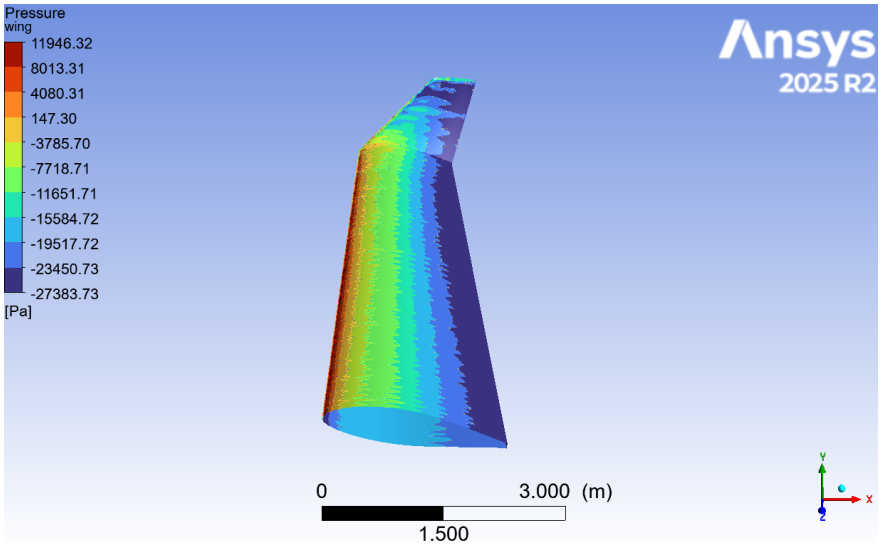


Figure 7.26: Pressure distribution over the 45-45 winglet configuration at 10° angle of attack.

Compared to the baseline wing at 0°, the magnitude of the minimum pressure increased by 2.48%, while the magnitude of the maximum pressure remained mostly the same. Due to the disproportionate increase in C_L, the layout of the pressure distribution correlated to this increase.

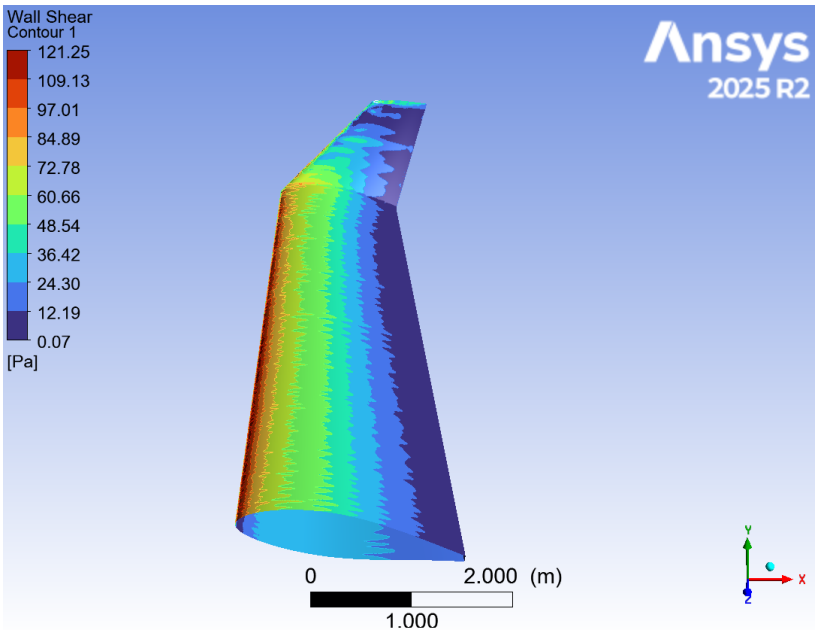


Figure 7.27: Wall-shear-stress distribution over the 45-45 winglet configuration at 10° angle of attack.

At 10° angle of attack, the change in wall-shear behavior was small, as the maximum wall shear stress decreased from 123.54 Pa for the baseline wing to 121.25 Pa for the conventional winglet. Similarly to the baseline, the highest wall shear stress occurred near the leading edge and decreased toward the trailing edge. The winglet also changed the wall shear distribution around the winglet.

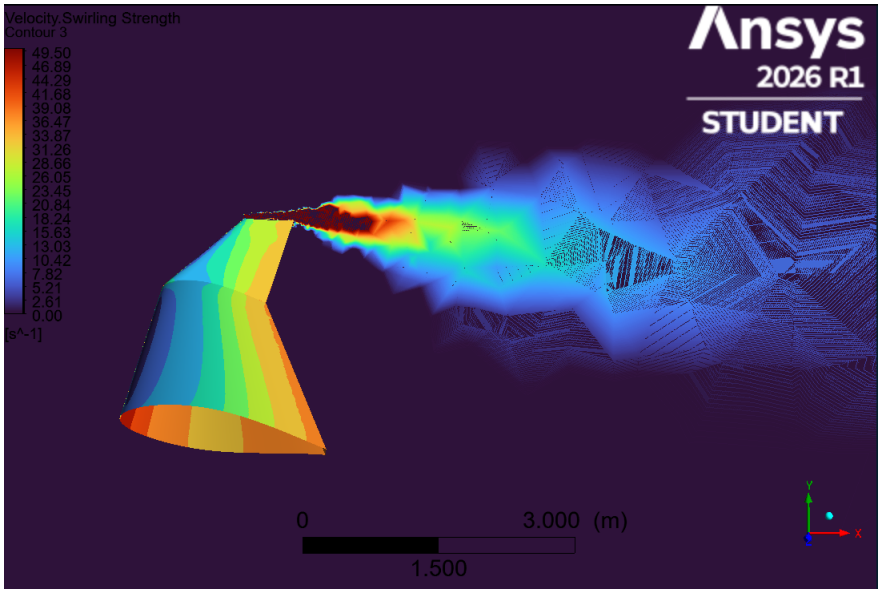


Figure 7.28: Swirling-strength contour of the near-tip wake for the conventional-winglet configuration at 10° angle of attack.

The wake at the tip of the conventional winglet at 10° had significantly decreased in size in

comparison to the baseline wing at 10°. The aerodynamic efficiency improved from the baseline wing at 10° from 18.432 to 19.552, mostly due to an increase in C_L. The more concentrated regions of higher swirling strength suggested a potential decrease in C_D, albeit a marginal amount.

7.7 45-45 Blended-Winglet Configuration at 0° Angle of Attack

At 0° angle of attack, the blended-winglet configuration produced a lift coefficient of C_L=0.15534 and C_D=0.015942. The L/D was 9.744, which was approximately 4.3% lower than the conventional winglet. The C_L increased by 1.8%, but C_D also increased by 6.4%. Since C_D increased significantly more than C_L, the aerodynamic efficiency decreased in comparison to previous configurations.

Table 7.7: Aerodynamic coefficients for the 45-45 blended-winglet configuration at 0° angle of attack.

Coefficient	**Value**
Lift coefficient, C_L	0.15534
Drag coefficient, C_D	0.015942
Lift-to-drag ratio, L/D	9.744

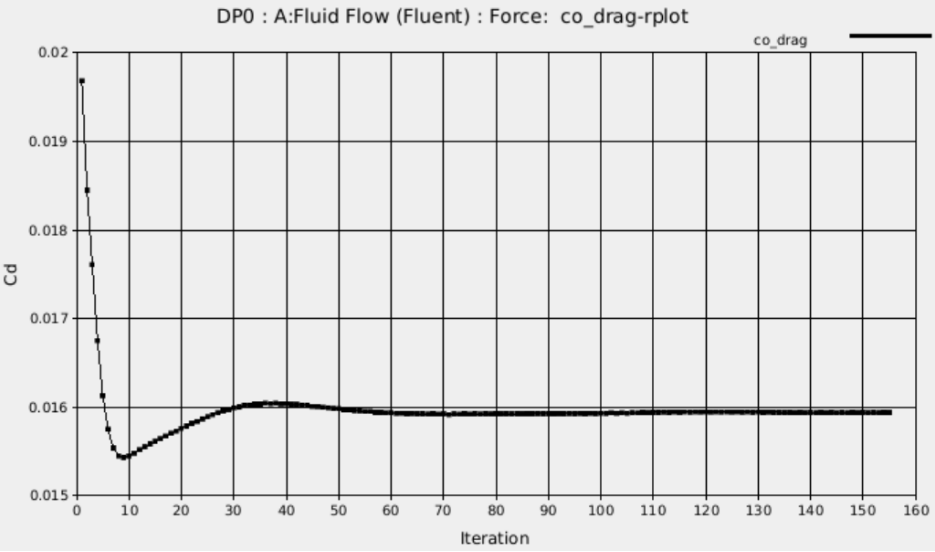


Figure 7.29: Drag-coefficient convergence history for the 45-45 blended-winglet configuration at 0° angle of attack.

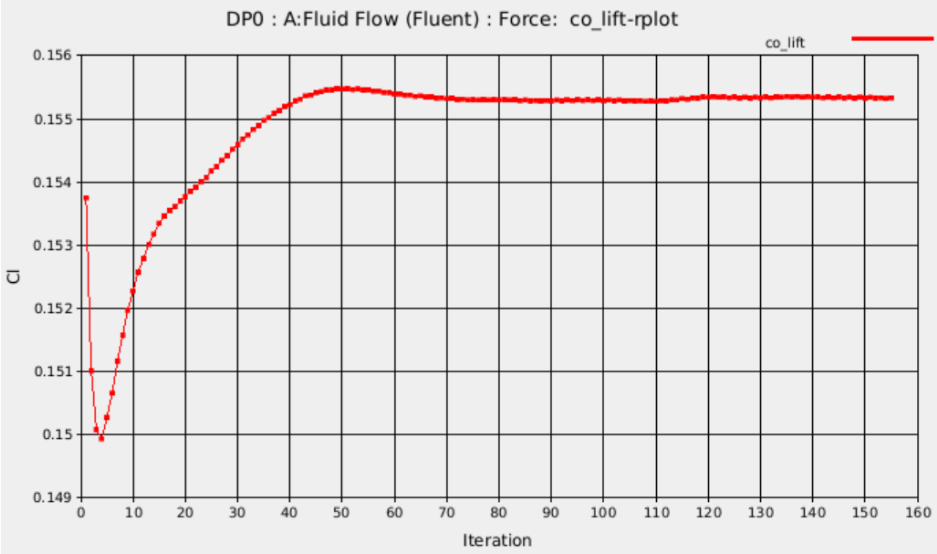


Figure 7.30: Lift-coefficient convergence history for the 45-45 blended-winglet configuration at 0° angle of attack.

Table 7.8: Aerodynamic coefficients for the 45-45 blended-winglet configuration at 0° angle of attack.

Aerodynamic quantity	**Value**
Lift coefficient, C_L	0.1553
Drag coefficient, C_D	0.01594
Lift-to-drag ratio, L/D	9.74

The pressure for the blended winglet configuration ranged from -8.95×10^3 Pa to 1.14×10^4 Pa. The minimum pressure difference was 0.05%, and the maximum pressure of the blended winglet was 2.34% lower than the conventional configuration.

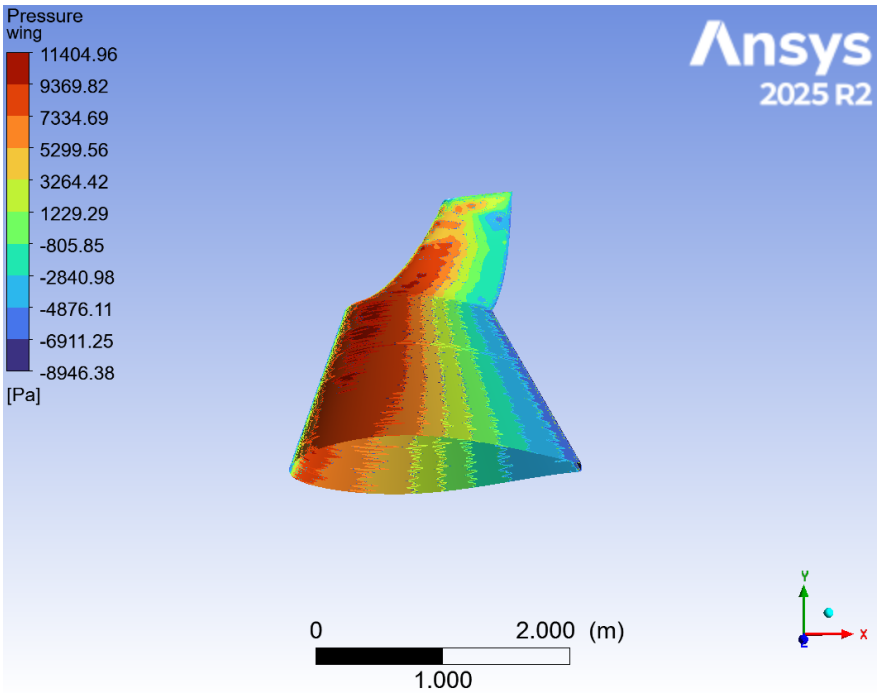


Figure 7.31: Pressure contour for the 45-45 blended-winglet configuration at 0° angle of attack.

Although the minimum-pressure magnitudes were nearly identical, the blended winglet produced a slightly higher lift coefficient due to a larger surface area. The higher C_D may have been due to pressure changes in the wingtip flow as a result of the curved design of the winglet.

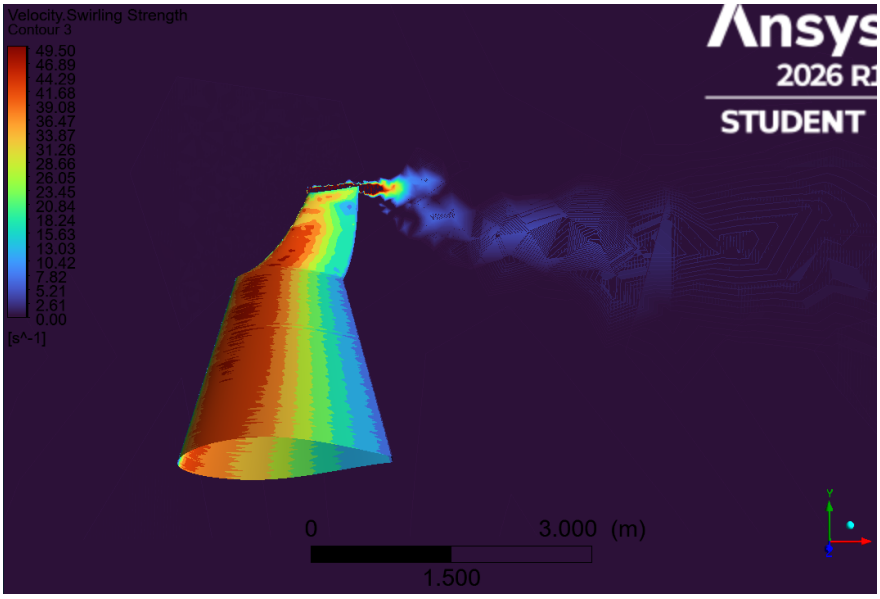


Figure 7.32: Swirling-strength contour of the near-tip wake for the blended-winglet configuration at 0° angle of attack.

The wake of the blended winglet produced a more compact wake and the vorticity strength was

weakest at the end of the wake compared to the 0° of the conventional winglet. However, this did not correspond to the increase in C_D. This demonstrated that the increase in aerodynamic efficiency could stem from other sources.

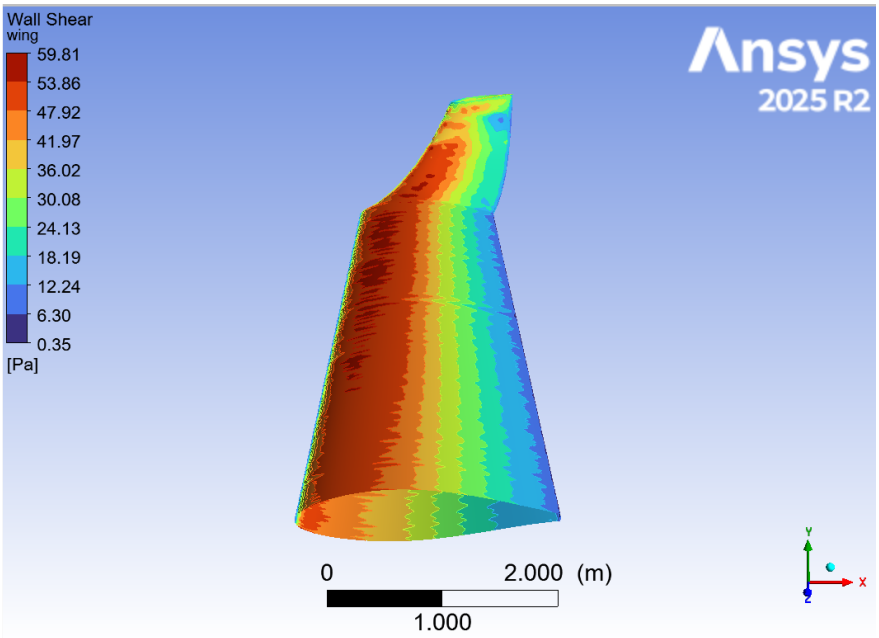


Figure 7.33: Wall shear stress contour for the 45-45 blended-winglet configuration at 0° angle of attack.

At 0° angle of attack, the maximum value was lower than that of the conventional winglet. This indicated that the the smoother wing-winglet junction from the blended winglet changed the near wall flow in this particular area.

7.8 45-45 Blended-Winglet Configuration at 6° Angle of Attack

The blended winglet configuration at 6° produced C_L=0.77582, C_D=0.034202, and L/D=22.683. The C_L of this configuration was 0.75% lower than C_L of conventional winglet, and C_D was 3.3% higher than the conventional winglet. As a result, the L/D was 3.3% lower. The L/D at 6° increased by 132.8% compared to the 0° case.

Table 7.9: Aerodynamic coefficients for the 45-45 blended-winglet configuration at 6° angle of attack.

Coefficient	**Value**
Lift coefficient, C_L	0.77582
Drag coefficient, C_D	0.034202
Lift-to-drag ratio, L/D	22.683

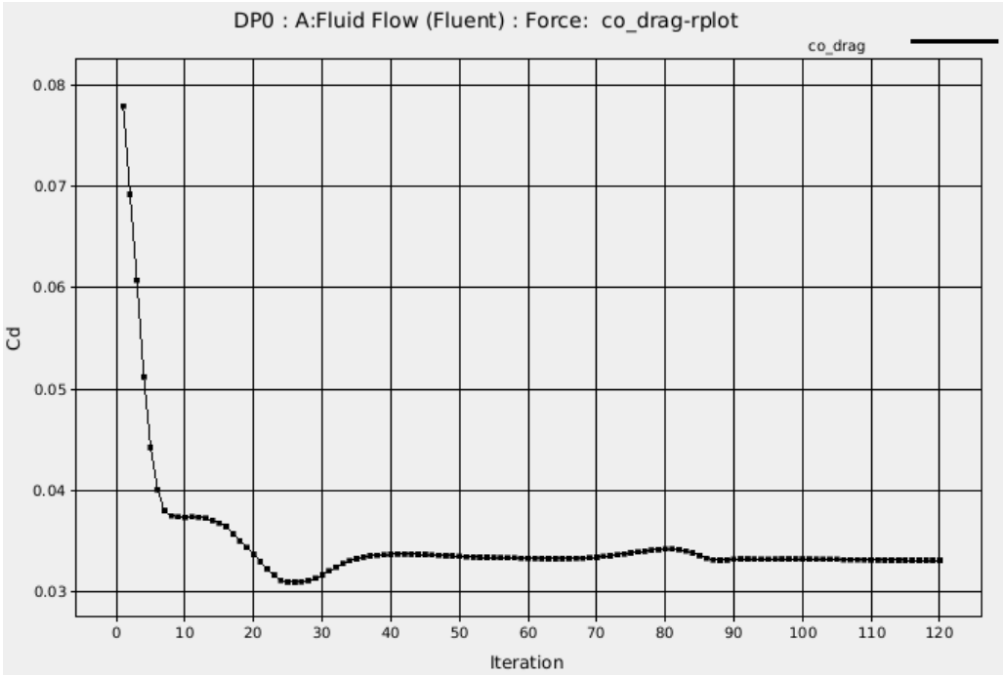


Figure 7.34: Drag-coefficient convergence history for the 45-45 blended-winglet configuration at 6° angle of attack.

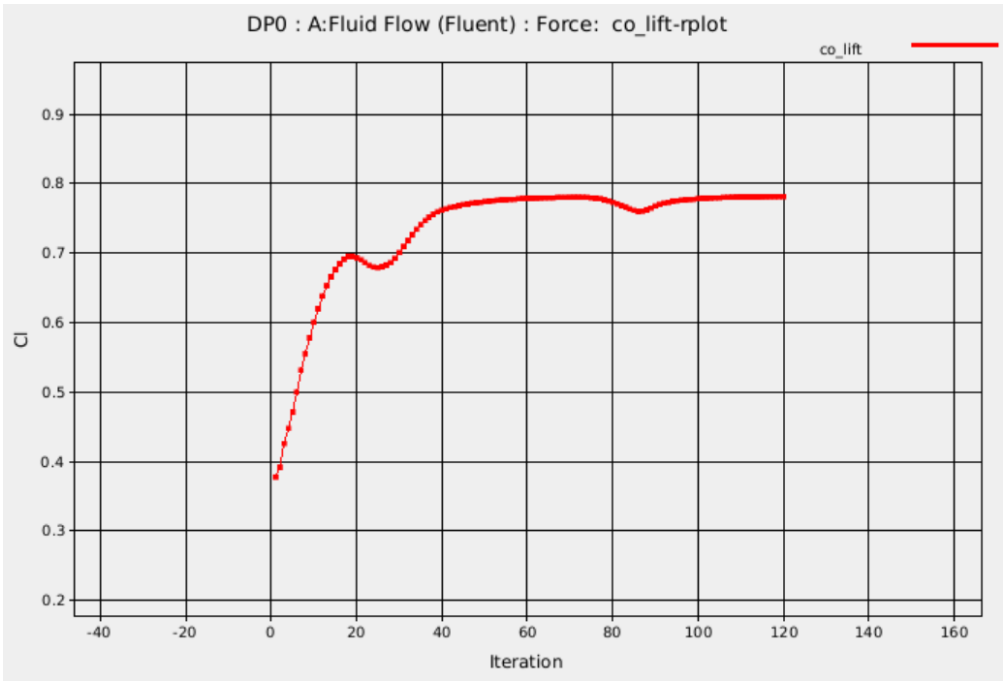


Figure 7.35: Lift-coefficient convergence history for the 45-45 blended-winglet configuration at 6° angle of attack.

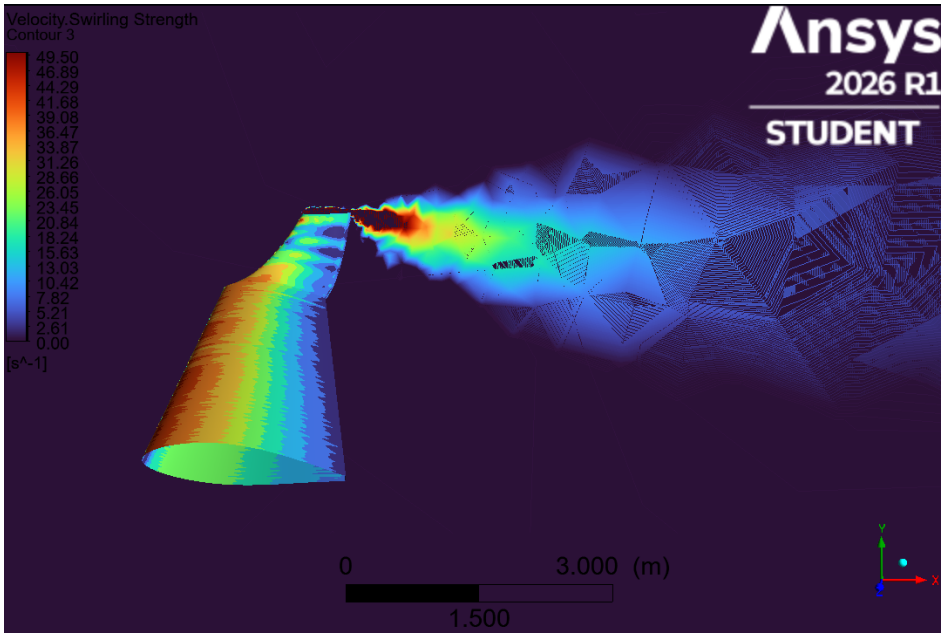


Figure 7.36: Swirling-strength contour of the near-tip wake for the blended-winglet configuration at 6° angle of attack.

At 6°, the blended winglet configuration exhibited a wake larger in size, which was consistent with a higher C_D. This may have been associated with the curvature and maintaining the same height of the winglet as the conventional configuration which altered the pressure distribution at the tip of the winglet. The blended winglet had a lower L/D as well.

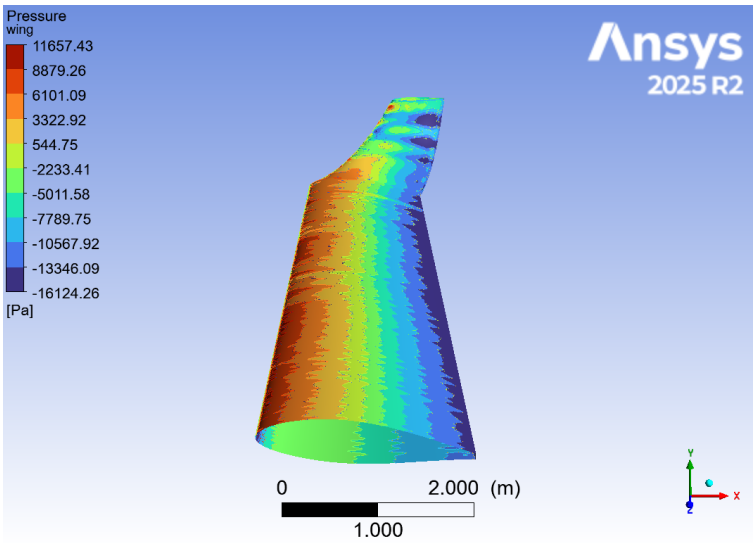


Figure 7.37: Pressure distribution over the 45-45 blended-winglet configuration at 6° angle of attack.

The pressure of the blended winglet configuration at 6° ranged from -1.61×10^4 Pa to 1.17×10^4 Pa. The maximum pressure decreased by 0.44% in comparison to the conventional winglet,

and the magnitude of the maximum pressure increased by 10.8%. Despite an increase in suction, C_L decreased by 0.75% as the suction occured at a single location instead of a larger surface area. This resulted in a lack of pressure across the wing which resulted in weaker lift generation. C_D also increased by 3.31%, which correlated with a 3.93% decrease in L/D.

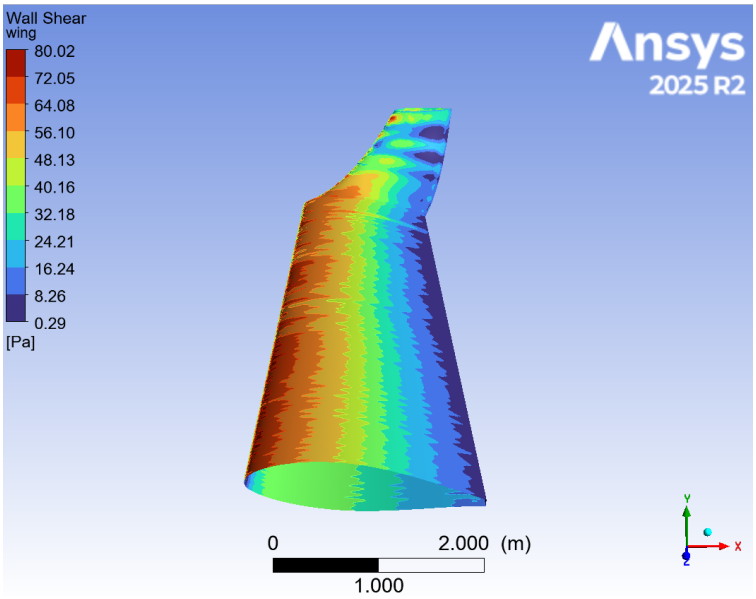


Figure 7.38: Wall-shear-stress distribution over the 45-45 blended-winglet configuration at 6° angle of attack.

The wall shear stress for the conventional-winglet configuration at 6° ranged from approximately 0.14 Pa to 85.98 Pa. The highest values occurred near the leading edge and decreased toward the trailing edge. Compared with the baseline wing at the same angle of attack, the maximum wall shear stress increased by only 0.56%, indicating that the peak near-wall velocity gradient remained nearly unchanged. The lower minimum value indicated a local region of flow momentum close to the surface.

7.9 45-45 Blended-Winglet Configuration at 10° Angle of Attack

The blended-winglet configuration at 10° generated values of C_L = 1.03195 and C_D = 0.063848. The L/D was subsequently 16.163. Relative to the conventional winglet, the blended configuration produced 9.6% less lift and 9.4% more drag, setting the L/D to be 17.3% lower.

Table 7.10: Iteration-averaged aerodynamic coefficients for the 45-45 blended-winglet configuration at 10° angle of attack.

Coefficient	**Value**
Mean lift coefficient, $\overline{C_L}$	1.03195
Mean drag coefficient, $\overline{C_D}$	0.063848
Mean lift-to-drag ratio, L/D	16.163

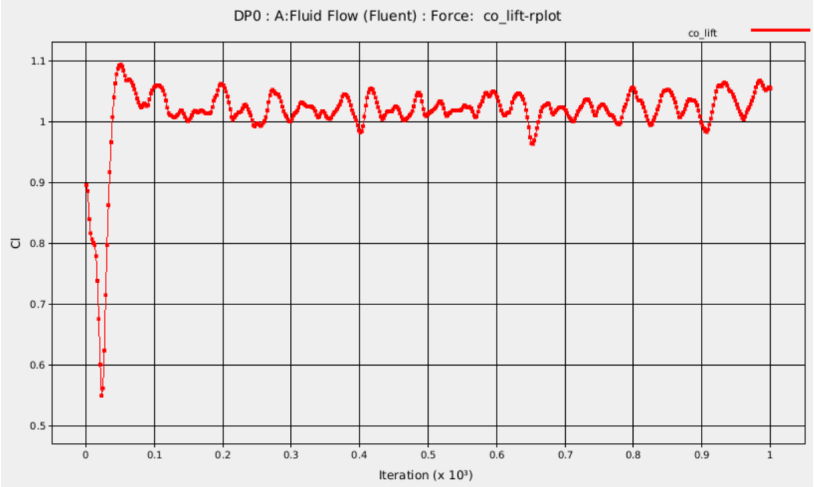


Figure 7.39: Lift-coefficient iteration history for the 45-45 blended-winglet configuration at 10° angle of attack.

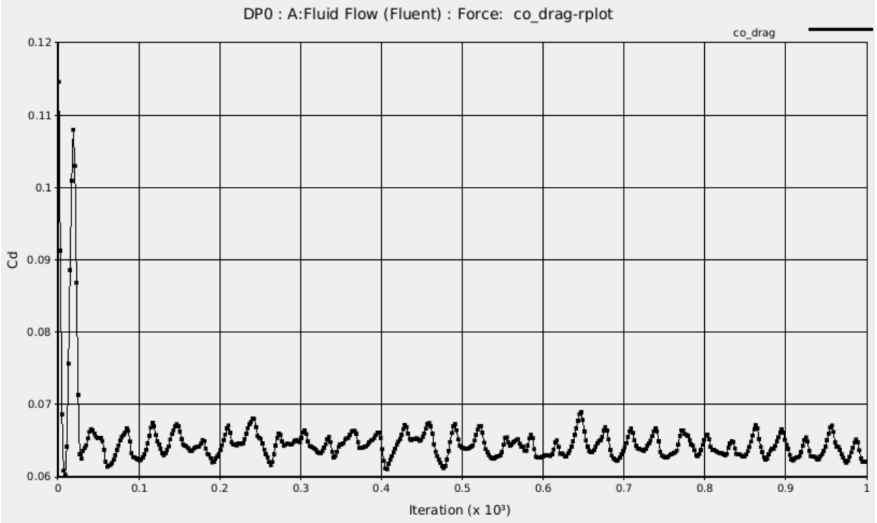


Figure 7.40: Drag-coefficient iteration history for the 45-45 blended-winglet configuration at 10° angle of attack.

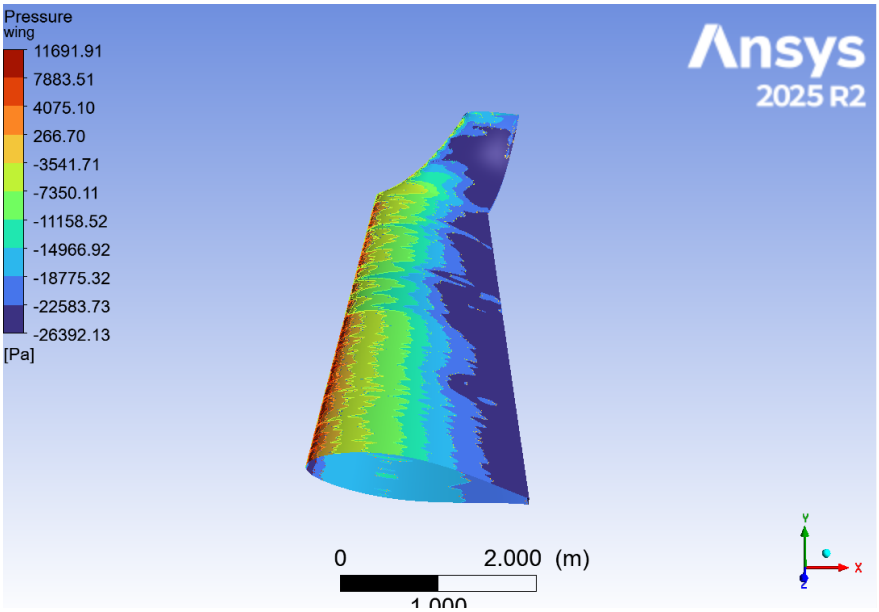


Figure 7.41: Pressure distribution over the 45-45 blended-winglet configuration at 10° angle of attack after 1000 iterations.

The pressure for the blended winglet at 10° varied from -2.64×10^4 Pa to 1.17×10^4 Pa. The maximum pressure decreased by 2.13% in comparison to the conventional winglet, and the magnitude of minimum pressure decreased by 3.62%. The weaker suction correlated to the decrease in C_L.

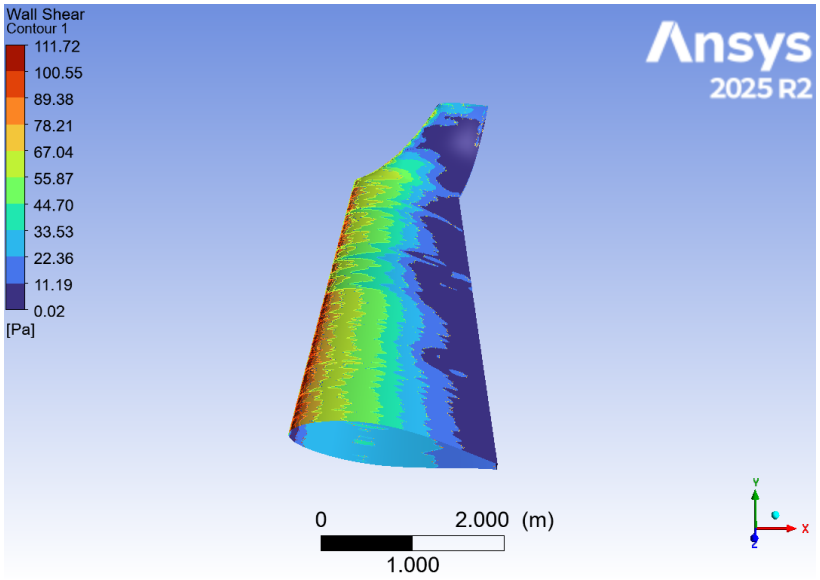


Figure 7.42: Wall-shear-stress distribution over the 45-45 blended-winglet configuration at 10° angle of attack after 1000 iterations.

The blended winglet at 10° angle of attack generated maximum wal shear stress of 111.72 Pa. This was 7.9% lower than the conventional winglet. The blended winglet also demonstrated

more irregular wall-shear stress distribution near the wingtip. There was lower pressure around the winglet, which may have suggested greater possibility toward disturbed or separated flow.

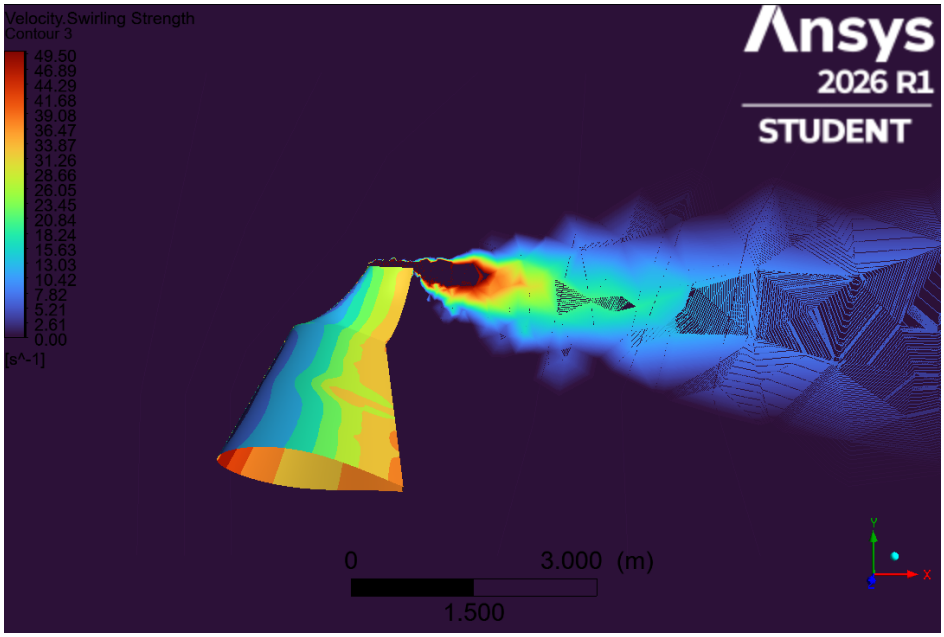


Figure 7.43: Swirling-strength contour of the near-tip wake for the blended-winglet configuration at 10° angle of attack.

The blended winglet had a more compact high-strength core near the tip than the conventional configuration. This was followed by a faster transition to regions of less strength. However, the blended winglet had a higher total C_D, which could possibly have been a result of additional pressure, viscous, or geometric effects.

7.10 Overview of Results

The conventional winglet configuration increased the C_L by 5.1% relative to baseline wing, and drag coefficient is increased by 4.9%. As a result, L/D is increased by only 0.22%.

Table 7.11: Comparison of aerodynamic coefficients for the baseline, 45-45 winglet, and 45-45 blended-winglet configurations at 0° angle of attack.

Configuration	**AOA**	C_L	C_D	L/D
Baseline	0°	0.14519	0.014293	10.158
45-45 winglet	0°	0.15260	0.014989	10.180
45-45 blended winglet	0°	0.15530	0.015940	9.743

However, both winglet configurations also produced higher drag than the baseline wing. The C_L of blended winglet increased by 7% compared to the baseline wing. However, C_D increased by 11.5%, leading to a lower L/D ratio. The blended winglet overall produced more drag than the

conventional configuration. Overall, the conventional winglet has the best aerodynamic efficiency at 0°, albeit a small improvement.

Table 7.12: Comparison of aerodynamic coefficients for the baseline, 45-45 winglet, and 45-45 blended-winglet configurations at 6° angle of attack.

Configuration	**AOA**	C_L	C_D	L/D
Baseline	6°	0.72537	0.033054	21.945
45-45 winglet	6°	0.78168	0.033105	23.612
45-45 blended winglet	6°	0.77582	0.034202	22.683

At 6° angle of attack, both winglet configurations led to greater aerodynamic efficiency in comparison to the baseline wing. The conventional winglet increased lift by about 7.8%, and the $C_D$increased only about 0.15%. As a result, the L/D ratio increased by 7.6%. The blended winglet also had an improvement of about 7%, and C_D increased by 3.5%, which led to a lower L/D ratio. The conventional winglet has shown to be the most aerodynamically efficient at an angle of attack of 6°.

Table 7.13: Comparison of aerodynamic coefficients for the baseline, 45-45 winglet, and 45-45 blended-winglet configurations at 10° angle of attack.

Configuration	**AOA**	C_L	C_D	L/D
Baseline	10°	1.0719	0.058153	18.432
45-45 winglet	10°	1.1414	0.058377	19.552
45-45 blended winglet	10°	1.03195	0.063848	16.163

The configuration with the highest aerodynamic efficiency at 10° was the conventional winglet. In comparison to the baseline wing, the conventional winglet increased C_L by 6.5%. C_D only increased by 0.39%, and L/D had an increase of around 6.1%. The blended winglet produced approximately 3.73% less lift and 9.79% more drag than the baseline wing, resulting in a 12.31% reduction in L/D. At 10°, the conventional wing remained as most efficient aerodynamically.

8. Verification and Validation

Experimental aerodynamic measurements for the NACA 63-418 airfoil were selected as a benchmark for evaluating the numerical methodology. The experimental study conducted by Kruse et al. [19] tested the NACA 63-418 airfoil over Reynolds number 3×10^6 to 7×10^6.

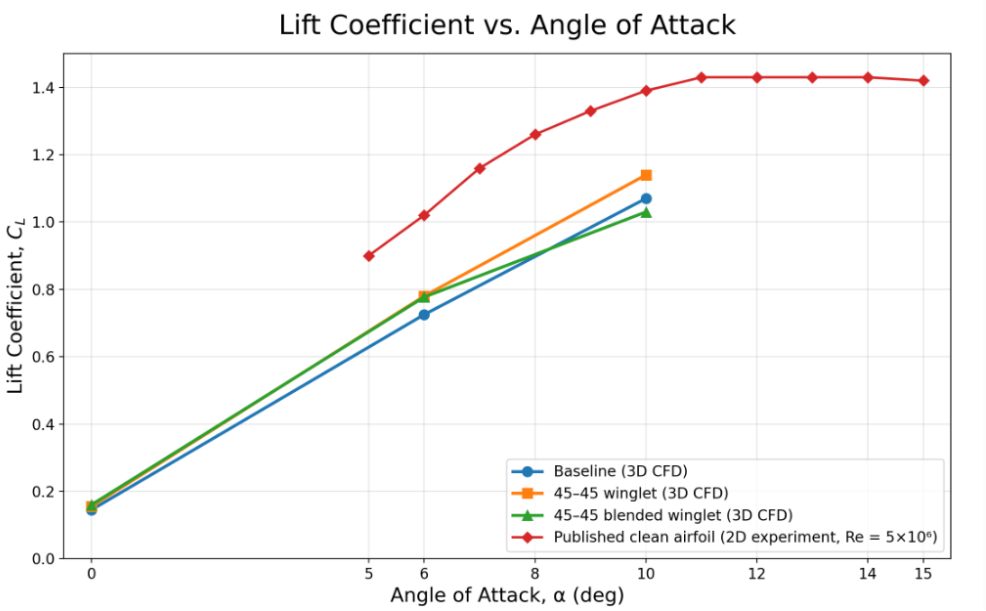


Figure 8.1: Comparison of lift coefficient as a function of angle of attack for the baseline wing, 45-45 winglet, and 45-45 blended-winglet configurations. Published clean NACA 63_3-418 airfoil wind-tunnel data at $Re = 5 \times 10^6$ were included as a qualitative reference. The published data represented a two-dimensional airfoil, whereas the CFD results represented three-dimensional finite-wing configurations.

Like the airfoil used for the simulations in this study, Kruse et al. [19] utilized the NACA 63-418 airfoil for their study on the aerodynamic effects of different types of surfaces. All three CFD configurations demonstrated a linear increase in lift coefficient with respect to angle of attack of the wing. This compared well with the published data, as the baseline wing lift curve slope was approximately 0.093 per degree and the lift curve slope for the study was around 0.086 per degree. The difference in C_L of the published study and of the baseline wing was due to the 2D simulation of the airfoil as well as different Reynolds number and Mach numbers. As a result, this comparison supported the qualitative validation of the physical lift trend of the CFD results.

In addition, meshing-sensitivity study was conducted to assess the influence of mesh resolution on aerodynamic coefficients and to observe if the results were not heavily influenced by the exact mesh settings. The convergence histories of the lift and drag coefficients for the baseline wing configuration at an angle of attack of 6° were presented in Figure 8.2. Both coefficients approached nearly constant values, indicating that the aerodynamic-force monitors stabilized.

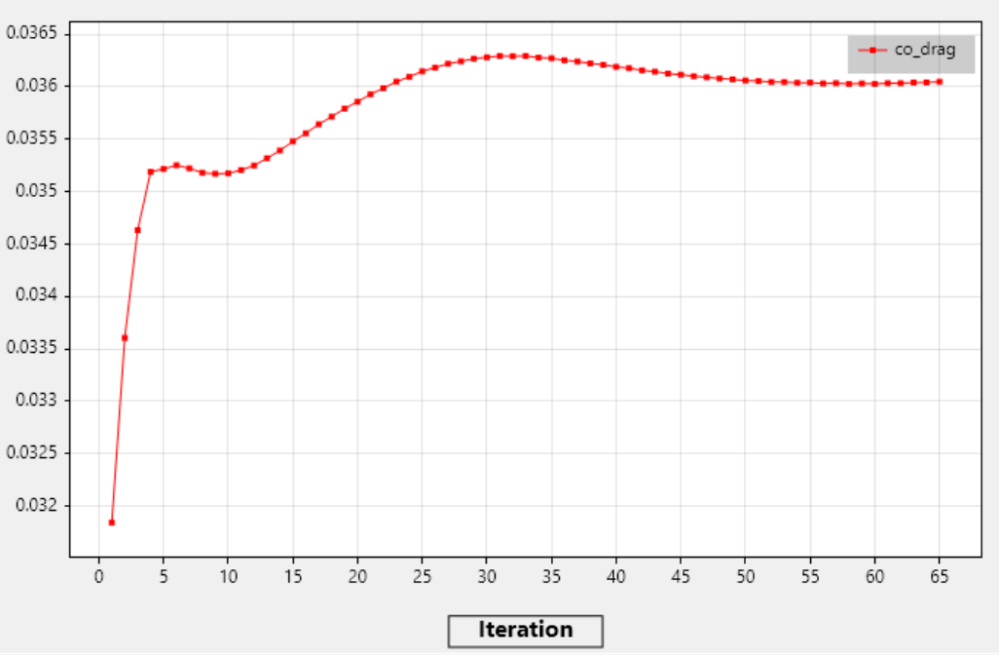


Figure 8.2: Drag coefficient convergence history for the baseline wing at 6° angle of attack.

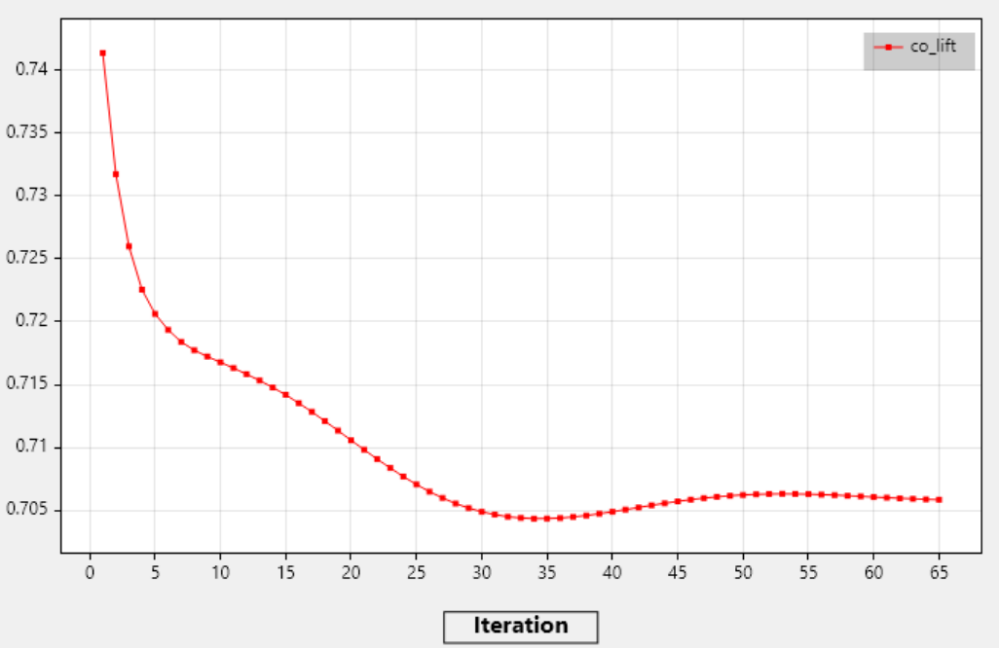


Figure 8.3: Lift coefficient convergence history for the baseline wing at 6° angle of attack.

For the baseline wing simulation at 6° angle of attack, the surface mesh was generated using an element size of 0.05 and a growth rate of 1.2. In addition, curvature-based refinement was enabled using the default curvature-normal angle of 18°. The inflation control used the first-layer-thickness option with a first-layer height of 1.0×10^{-3} m, a maximum of 15 layers, and a growth rate of 1.18.

The refined baseline case was then simulated at 6° angle of attack. The lift and drag coefficients

approached stable values after approximately 65 iterations. The drag coefficient stabilized near $C_D \approx 0.03604$, while the lift coefficient stabilized near $C_L \approx 0.70631$. Relative to the original simulation, the coarser mesh predicted an approximately 2.63% lower lift coefficient, a 9.03% higher drag coefficient, and a 10.70% lower lift-to-drag ratio. These differences indicated that the aerodynamic coefficients remained sensitive to mesh resolution and that complete mesh independence was not demonstrated.

9. Conclusion

This project evaluated the baseline wing, a conventional 45-45 winglet, and a blended 45-45 winglet at three angles of attack under the same freestream and reference area conditions. After all three configurations were simulated and analyzed, the conventional 45-45 winglet produced the highest L/D at every angle of attack. At 6°, the winglet increased L/D by 7.6%, producing the highest L/D, and at 10°, L/D increased by 6.1%. The increase in aerodynamic efficiency was more marginal at 0°.

The blended winglet was overall less efficient than the conventional winglet. The lift-to-drag ratio was approximately 3% higher than the baseline at 6°, although it was 4% lower than conventional winglet. Due to a large amount of drag at 0°, the lift-to-drag ratio was the smallest among the three configurations.

Although the purpose of the blended winglet was to reduce junction interference, the conventional 45-45 winglet produced the highest lift-to-drag ratio at all three angles of attack. This indicated that the curved structure or additional lift in the blended winglet case was insufficient in offsetting drag. This result may have been due to the specific blend geometry in this study rather than blended winglets in general. The large curved part of the winglet may have increased surface area and thickness, which could have increased drag. While the goal of the smooth transition may have been reduced interference, this was possibly outweighed by additional drag. A potential solution would be to increase the height of the blended winglet in order to strengthen the loading. On the other hand, there could be potential drawbacks, such as increasing the wetted area.

The contours generally matched the trends observed with the aerodynamic coefficients. As the angle of attack increased, the pressure difference between the upper and lower wing surfaces became larger, corresponding to the increase in lift. The wall-shear-stress contours also showed changes in the near-wall flow as the aerodynamic loading increased. In addition, the swirling-strength contours indicated that both winglet configurations redistributed the near-tip wake relative to the baseline wing. However, the presence of a modified wake structure did not necessarily result in improved overall aerodynamic efficiency in all cases. Among the configurations examined, the conventional 45-45 winglet provided the most favorable balance between aerodynamic loading and total drag, consistent with its higher lift-to-drag ratio at all three angles of attack. Although the blended winglet also altered the near-tip flow, its additional drag prevented it from achieving the same aerodynamic performance as the conventional winglet.

There were some limitations faced in this study. The aerodynamic coefficients for the blended-winglet configuration at 10° were obtained from values averaged by iteration because the solution did not reach a strict steady-state convergence. Moreover, because the available Ansys license imposed a limit on the allowable number of mesh elements, more mesh convergence studies were not able to be examined to observe potential mesh independence. This prevented more simulations with a medium-course mesh from being tested. Future work should also examine a redesign of the blended winglet with an increased winglet height. A further investigation of a broader range of cant and sweep angles to determine whether a larger or smaller wing-to-winglet angle provides aerodynamic benefits that outweigh additional viscous and interference drag would be useful.

References

[1] Sundaram, M. K., Teja, V. R., and Sai, B. S., "Study on Induced Drag Reduction of Electric Aircraft Wing Using Various Winglet Configurations: A Review," *Advances in Additive Manufacturing Technologies*, 2024.

[2] Lu, G., and Zhou, G., "Numerical Simulation on Performances of Plane and Curved Winglet-Pair Vortex Generators in a Rectangular Channel and Field Synergy Analysis," *International Journal of Thermal Sciences*, 2016.

[3] Hasan, A. Q., Al-Khudhiri, N. M., Iqbal, M. A., Dol, S. S., Azeez, A. A., and Gadala, M. S., "Aerodynamics Analysis on Wings with Winglets and Vortex Generators," *WSEAS Transactions on Fluid Mechanics*, Vol. 15, pp. 193-201, 2020. doi:10.37394/232013.2020.15.19.

[4] Babu, D. P. R., Madhesh, D., Hasan, I., and Mukesh, R., "Evaluation of Traditional and Slotted Winglets for Enhanced Aerodynamic Efficiency," *Physics of Fluids*, Vol. 37, No. 2, 2025, Article 023102. doi:10.1063/5.0252472.

[5] Madani, S. A. S., Vaezi, E., and Keshmiri, A., "CFD-Driven Evaluation of Winglet Cant Angle: Insights into Aerodynamic and Aeroacoustic Performance," *Results in Engineering*, Vol. 26, 2025, Article 104759. https://doi.org/10.1016/j.rineng.2025.104759.

[6] Farook, M. H., and Chitharanjan, V. K. G., "Corrugated Winglets Efficiency: A Numerical Study," *CFD Letters*, Vol. 17, No. 8, pp. 217-234, 2025. doi:10.37934/cfdl.17.8.217234.

[7] Guerrero, J. E., Sanguineti, M., and Wittkowski, K., "Variable Cant Angle Winglets for Improvement of Aircraft Flight Performance," *Meccanica*, Vol. 55, No. 8, pp. 1917-1947, 2020. doi:10.1007/s11012-020-01230-1.

[8] Malathi, S., Kamalakrishna, T. R., Ramakrishna, D., Sankaralingam, L., Saravanan, P., Saranya, K., and Seralathan, S., "Computational Study on Induced Drag Reduction of Electric Aircraft Wing Using Various Winglet Configurations," In *Recent Trends in Thermal and Fluid Sciences*, Springer Nature Singapore, 2024. doi:10.1007/978-981-97-5373-4_22.

[9] Pecora, R., Amoroso, F., Noviello, M. C., Dimino, I., and Concilio, A., "Aeroelastic Stability Analysis of a Large Civil Aircraft Equipped with Morphing Winglets and Adaptive Flap Tabs," *Proc. SPIE 10595*, 2018. doi:10.1117/12.2300173.

[10] Sheneshen, A. M., and Kamal, A. M., "Influence of Winglets Design Parameters on Aerodynamic and Stability of a Blended Wing-Body Aircraft," *Journal of Physics: Conference Series*, Vol. 3070, 2025, Article 012004. doi:10.1088/1742-6596/3070/1/012004.

[11] Heidari Soreshjani, M., and Jahangirian, A., "An Investigation on Winglet Design with Limited Computational Cost, Using an Efficient Optimization Method," *Aerospace Science and Technology*, Vol. 117, 2021, Article 106957. doi:10.1016/j.ast.2021.106957.

[12] Kim, U., *Numerical Analysis and Optimization of Wing-tip Designs*, Master's Project, Department of Aerospace Engineering, San Jose State University, 2015.

[13] Krebs, T. A., and Bramesfeld, G., "Using an Optimisation Process for Sailplane Winglet Design," *The Aeronautical Journal*, Vol. 120, No. 1233, pp. 1726-1745, 2016. doi:10.1017/aer.2016.83.

[14] NASA Glenn Research Center, "Drag Coefficient - Beginners Guide to Aeronautics," https://www.grc.nasa.gov/www-k-12/VirtualAero/BottleRocket/airplane/dragco.html.

[15] Eviation Aircraft Ltd., "Alice - The All-Electric Commuter Aircraft," https://www.eviation.com/aircraft/.

[16] Jane's All the World's Aircraft, "Cessna 525B Citation CJ3," Migavia, https://janes.migavia.com/usa/cessna/cessna-525b-citation-cj3.html, accessed 2 August 2026.

[17] Litherland, B., "NACA 6-Series Airfoil," *OpenVSP Ground School*, NASA Langley Research Center, Hampton, VA, 2024. https://vspu.larc.nasa.gov/training-content/chapter-1-vspfundamentals/cross-section-details/naca-6-series-airfoil/.

[18] AirfoilTools, "NACA 63-418 Airfoil," *AirfoilTools.com*, Retrieved 2025, http://airfoiltools.com/airfoil/details?airfoil=naca633418-il.

[19] Kruse, E. K., Bak, C., and Olsen, A. S., "Wind Tunnel Experiments on a NACA 63_3-418 Airfoil with Different Types of Leading-Edge Roughness," *Wind Energy*, Vol. 24, No. 11, pp. 1263-1274, 2021. doi:10.1002/we.2630.